POLITECNICO DI TORINO

Master's Degree in
Communications and Computer Networks Engineering

Master's Degree Thesis

# Study of high sensitivity GNSS receivers for space applications and lunar missions

Supervisors

**Prof. Fabio DOVIS**

**Dr. Alex MINETTO**

Candidate

**Margherita MARIANI**

Academic Year 2020/2021

# Abstract

Global Navigation Satellite System (GNSS) provides accurate Positioning, Navigation and Timing (PNT) information to the users. Originally, these have been designed to serve terrestrial users, but in the last years the interest in the use of GNSS for autonomous space navigation has significantly increased.
Over the past decades, space missions have leveraged Precise Orbit Determination (POD), which is the process of accurately estimating and tracking both position and velocity of spacecraft along the orbit. This method usually relies on post-processing computation, based on range and Doppler tracking services offered by federated networks (i.e. NASA Deep Space Network), managed by the ground segment. On the contrary, exploiting real-time, in-orbit GNSS-based navigation systems would make the spacecraft more autonomous, reducing the costs and the effort of ground operations. The use of in-orbit GNSS receivers has been validated in low orbits, as in Low Earth Orbits (LEOs), up to a distance of approximately 150.000 km from the Earth's surface. The use of GNSS in space applications is hence becoming attractive even for spacecraft navigation at larger distances, for example, in lunar missions. However, deploying GNSS receivers all the way to lunar distances is a challenging task due to multiple factors. First of all, the received signals are characterized by low power levels, especially at altitudes above the GNSS constellation. In these conditions, the signals transmitted by the main antenna lobes suffer occultation effects, being received from satellites orbiting on the opposite side of the Earth. Side lobes, on the other hand, only provide low-power signals in the spacecraft direction. Besides, signal availability is drastically impaired by poor geometry, leading to accuracy degradation in the positioning and navigation solutions. Additionally, GNSS space-born receivers could experience high relative dynamics with respect to the GNSS satellites, which are responsible for both Doppler frequency and Doppler rate.

This thesis work aims at studying and implement techniques allowing to increase the sensitivity of GNSS space-born receivers, so that to acquire very weak signals in non-terrestrial applications. The targeted strategies involve the extension of the integration time in the acquisition stage, to accumulate signal energy and cope with low Carrier-to-Noise density ratio ($C/N_0$). However, by increasing the

integration time interval, the effect of the Doppler frequency on the signal gets enhanced and weakens the acquisition sensitivity improvement ensured by these techniques. Doppler shift impacts on acquisition performance by affecting both the carrier and the code, resulting in carrier Doppler and code Doppler. Therefore, a key requirement in space missions is to have an accurate estimation of the Doppler frequency so that to compensate for it to a certain extent. The Doppler estimate is of great importance to reduce the dimension of the Search Space (SS) as well, in terms of Doppler frequency bins to be explored. In particular, not only the Doppler frequency shift must be taken into account, but also its change over time, namely the Doppler frequency rate. For this purpose, an adaptive Orbital Filter (OF), exploiting an Extended Kalman Filter (EKF), can supply signal frequency estimation, thus aiding both the acquisition and the tracking stages. Results about the impact of the Doppler on the acquisition performance are presented, together with the proposed compensation of these effects.

Both Doppler compensation and high-sensitivity acquisition techniques have been validated through a GNSS software receiver. Specifically, a real scenario has been analysed about a lunar mission in the framework of the Lunar GNSS Receiver Experiment (LuGRE). This project focuses on an experimental assessment of the performance of a GNSS receiver to support cis-lunar and lunar navigation. The addressed scenario foresees a constraint on the extension of the integration time, due to a set of technical mission constraints. Considering this limitation, an analysis regarding the acquisition performance has been carried out. In particular, given the limited signal length, it has been investigated which is the best number of Doppler frequency bin $N_D$ and which is the best acquisition decision logic, in terms of false alarm probability, to acquire signal at different $C/N_0$ levels, corresponding to different points along the Moon Transfer Orbit (MTO). Finally, a discussion will follow about the proper number of Doppler frequency bins and the false alarm probability, related to the accuracy of the Doppler frequency estimates provided by the OF.

# Table of Contents

# List of Tables

# List of Figures

# Acronyms

**ADC** Analogue-to-Digital Conversion

**AGC** Automatic Gain Control

**ASI** Agenzia Spaziale Italiana

**BDS** BeiDou Navigation Satellite System

**CAF** Cross-Ambiguity Function

**CCF** Cross-Correlation Function

**CDMA** Code Division Multiple Access

$C/N_0$ Carrier-to-Noise density ratio

**DFT** Discrete Fourier Transform

**DLL** Delay-Locked Loop

**DoD** Department of Defence

**DSN** Deep Space Network

**DSP** Digital Signal Processing

**DSSS** Direct-Sequence Spread Spectrum

**ECEF** Earth-Centered Earth-Fixed

**EKF** Extended Kalman Filter

**ESA** European Space Agency

**EU** European Union

**FDMA** Frequency Division Multiple Access

**FFT** Fast Fourier Transform

**FLL** Frequency-Lock Loop

**GEO** Geostationary-Earth Orbit

**GLONASS** Globalnaya Navigazionnaya Sputnikovaya Sistema

**GNSS** Global Navigation Satellite System

**GPS** Global Positioning System

**IEEE** Institute of Electrical and Electronics Engineers

**IF** Intermediate Frequency

**IFFT** Inverse Fast Fourier Transform

**IGSO** Inclined Geosynchronous Orbit

**LEO** Low Earth Orbit

**LOS** Line-of-sight

**LS** Least-Squares

**LuGRE** Lunar GNSS Receiver Experiment

**MMS** Magnetospheric Multiscale

**MEO** Medium Earth Orbit

**ML** Maximum Likelihood

**MTO** Moon Transfer Orbit

**NASA** National Aeronautics and Space Administration

**NEIL** Navigation Early Investigation on Lunar surface

**OF** Orbital Filter

**p.d.f.** Probability Density Function

**PLL** Phase-Locked Loop

**PNT** Positioning, Navigation and Timing

**POD** Precise Orbit Determination

**PRN** Pseudo Random Noise

**PVT** Position, Velocity, Timing

**RE** Radius Earth

**RF** Radio Frequency

**r.v.** random variable

**SDR** Software-Defined Radio

**SIS** Signal-in-Space

**SNR** Signal-to-noise ratio

**SS** Search Space

**SSV** Space Service Volume

**STK** Systems Tool Kit

**ToA** Time-of-Arrival

**TTFF** Time To First Fix

**U.S.** United States

**VLBI** Very Long Baseline Interferometry

**WGN** White Gaussian Noise

**WLS** Weighted-Least-Squares

# Chapter 1

# Introduction on GNSS

Global Navigation Satellite System (GNSS) is a constellation of satellites continuously transmitting radio signals providing accurate positioning and timing information to the receivers. The latter can use these information to determine their position, velocity and time. By definition, a global navigation satellite system provides global coverage on the Earth surface.
Each navigation system mainly consists of three segments:

- The Space Segment, which involves the constellation of spacecraft in orbit sending the radio signals;
- The Control Segment, dealing with the monitoring and management of the constellation of satellites;
- The User Segment, composed by the GNSS receivers determining their own position.

Among the fully operational GNSSs, the first one to be developed is the Global Positioning System (GPS), owned by the United States (U.S.) government and operated by the United States Space Force. The baseline nominal constellation consists of 24 spacecraft, distributed over six orbital planes equally spaced and with inclination at 55 degrees with respect to the equatorial plane. To ensure the visibility of at least four satellites from any point of the Earth, each plane contains four baseline satellites. Over the years, new spacecraft have been added to improve the performance of GPS. At the time of writing, GPS space segment is composed by 31 operational satellites [1], placed in Medium Earth Orbit (MEO) at an altitude of about 20,200 km and with a nominal orbital period of about 12 hours. Therefore, these satellites revolve around the Earth roughly twice a day [2].
Based on the same principles of the GPS, there is the Globalnaya Navigazionnaya Sputnikovaya Sistema (GLONASS) constellation, developed by the Sovietic Union.

GLONASS space segment is composed of 24 operational satellites arranged over three orbital planes, resulting in eight satellites for each plane. These satellites operate in circular orbits at an altitude of 19,100 km and an inclination of 64.8 degree. The high inclination is thought as to serve high latitude regions with a proper coverage. Similarly to GPS constellation, each spacecraft completes an orbit in about 11 hours and 15 minutes [3].
The European Union (EU), together with the European Space Agency (ESA) have developed the GALILEO satellite navigation system. It consists of 30 satellites placed at 23,222 km in MEO orbit, with 10 satellites in each of the 3 orbital planes, having inclination at 56 degrees. These satellites have a period of 14 hours 4 minutes 42 seconds [4].
China's BeiDou Navigation Satellite System (BDS) instead, is characterized by a constellation including 5 Geostationary-Earth Orbit (GEO) satellites, 27 in MEO and 3 in Inclined Geosynchronous Orbit (IGSO), leading to a total of 35 satellites [5].

## 1.1 Radionavigation principles

The determination of the position and of the velocity of a user is made by means of radio navigation, so estimating parameters of an electromagnetic wave. Specifically, GNSS exploits the Time-of-Arrival (ToA) of the received signals to determine the distances between the receiver and transmitters. The position of the latter can be derived from the navigation data. Then, the user location is obtained intersecting spheres. This process is referred to as trilateration.
Depending on which parameters of the signal are estimated, different positioning systems are used. GNSS is based on the measurement of the ToA of radio signals propagation and it exploits a spherical system. Fig.1.1 shows the 2-D positioning system using circles as LOP. The receiver, located in point P, measures its distance from the centre of each LOP, corresponding to the known positions of satellites $S_1 = (x_1, y_1, z_1)$, $S_2 = (x_2, y_2, z_2)$ and $S_3 = (x_3, y_3, z_3)$. Therefore, the range between the user and each transmitter corresponds to the radius $r_{1,2,3}$ of each circle. These ranges give information only about distances, so the receiver can be located in any point of each circle. The position P is obtained by intersection of circles.

The radius of the circles, corresponding to the geometrical distance between the receiver and the transmitters, can be estimated as:

$$R = c(T_{RX} - T_{TX}) = c\tau \tag{1.1}$$

where $c$ is the speed of light, $T_{TX}$ is the time instant at which the satellites transmit the signal, $T_{RX}$ is the time instant at which the signal is received by the user and therefore $\tau$ is the signal propagation time. To be able to make this computation, is

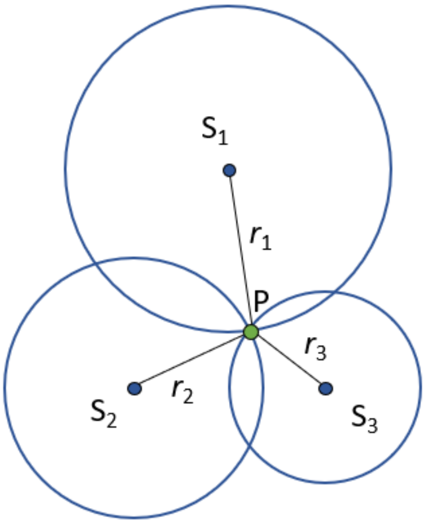

**Figure 1.1:** Trilateration - 2-D system

necessary that both the user clock and the GNSS satellites are aligned with GNSS time-scale. However, having receiver and transmitters clock synchronised with high precision is complex and costly. Hence, a bias $\delta t_u$ between the user clock and the satellite time-scale is taken into account. The measured distance is therefore different with respect to the geometrical one and it is called pseudorange:

$$\rho = c\tau + c \cdot \delta t_u = c\tau + b_u \tag{1.2}$$

As can be seen from (1.2), the user clock bias is multiplied by the speed of light, thus, even a small misalignment generates a great difference between the pseudorange and the geometrical distance. This bias is an additional unknown beside the user three-dimensional location $P = (x_u, y_u, z_u)$. This means that, in order to determine the 4 unknowns, the user must be able to measure 4 pseudoranges, which means that at least 4 satellites must be in view and in Line-of-sight (LOS) with the receiver. Anyway, the more the satellites in view, the better is the satellites geometry and the more precise is the position measurement. Actually, even the on board clock of the satellite might be slightly misaligned with respect to the GNSS time-scale. Still, this bias is stable in time and it is constantly monitored by ground stations, thus, it can be corrected.

In order to estimate the vertical component of position too, the problem must be extended to 3-D positioning. For this purpose, a spherical positioning system is used, where the user position is obtained by the intersection of spheres instead of circles. The latter is a simple enough extension, in mathematical terms, with respect to what analysed in the 2-D system.

## 1.2 GNSS Signal-in-Space

The signal continuously broadcasted by GNSS satellites is called Signal-in-Space (SIS). Each SIS is generated exploiting one or more Radio Frequency (RF) carriers, that are RF sinusoidal voltages produced by the transmitter at a specific frequency. As shown in Fig. 1.2, the majority of GNSS signals are transmitted using frequencies on the L-band, whose range is defined by the Institute of Electrical and Electronics Engineers (IEEE) to be from 1 to 2 GHz [6].

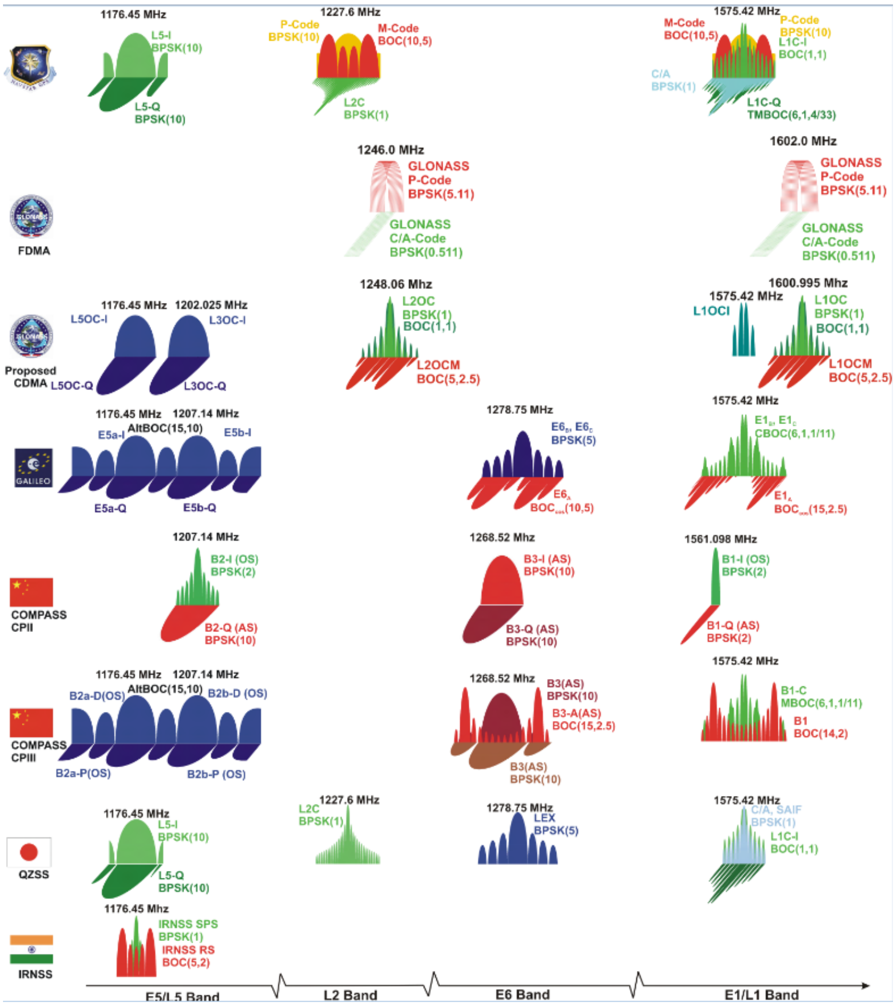

**Figure 1.2:** GNSS frequency bands. Source: [7]

This band provides advantages, with respect other frequency bands, in terms of delays and robustness with respect to attenuation caused by Earth's atmosphere and by precipitations.
Besides the carrier, SIS signals are mainly composed by the ranging code and the navigation data. The ranging codes, also denoted as Pseudo Random Noise (PRN) codes, are sequences of zeros and ones with great mathematical properties, which allow the transmission of several signals at the same time and on the same frequency, without interference. In addition, these codes are exploited by the receiver to estimate the pseudo-distance between user and spacecraft, therefore to compute the propagation time of the signal transmitted by the satellite. Concerning the navigation data, these are binary-coded messages which provide information about the satellite such as its health status, clock bias, ephemeris (position and velocity of the satellite itself) and almanac (ephemeris, with reduced accuracy, of all the satellites of the constellation) [7].

### 1.2.1 Modulation and Multiplexing technique

Most of the GNSS signals are modulated exploiting the Direct-Sequence Spread Spectrum (DSSS) technique. This modulation allows to reduce interference and improves signal robustness. In particular, the signal is spread in frequency through a multiplication with a sequence of chips, which are rectangular pulses with amplitude +1 or -1. This technique is illustrated in Fig.1.3 where, besides being modulated by the navigation data waveform, the RF carrier is modulated with a spreading waveform generated through a PRN code, also called spreading code or ranging code. All these components are synchronized, meaning that the beginning of the period of the carrier exactly coincides with the starting point of the code chip and of the data bit.

Most of the GNSS constellations exploit these ranging codes to implement Code Division Multiple Access (CDMA) channel sharing technique. In CDMA, all the transmitters can send signals simultaneously over the same frequency. In fact, flows separation is done by means of codes, exploiting spread spectrum technology. A given code is assigned to each transmitter and it must be known at the receiver. Then, both at the transmitter and at the receiver, a scalar product between the information bit and the specific code is done. Since the employed codes are orthogonal, the product is equal to 1 only for the signal coming from the transmitter corresponding to that specific code. On the contrary, for all the other signals this product is equal to 0. Therefore, even if all signals transmitted over the same channel sum up, they can be easily distinguished at the receiver through correlation.
GNSS using CDMA assign a unique PRN code to each satellites. The receivers know all these codes and they are able to separate and detect the signal transmitted

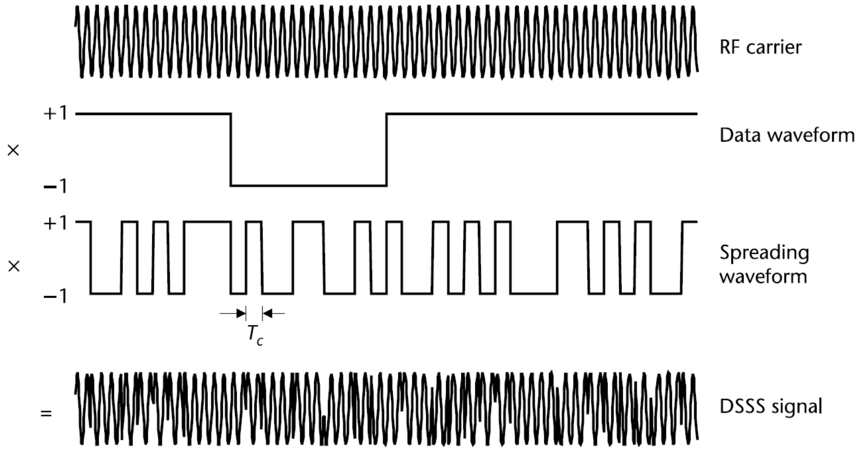

**Figure 1.3:** Direct Sequence Spread Spectrum modulation. Figure not to scale. Source: [6]

by the satellite of interest from the other ones. This multiplexing technique is used by Beidou, Galileo and GPS, while GLONASS exploits Frequency Division Multiple Access (FDMA), which means that all satellites transmit the same code on different frequencies.

### 1.2.2 GPS signal

In this thesis work just GPS signals have been used, therefore here follows a focus on their characteristics and their components. Anyway, it is due specifying that this not limit the generality of the study. Indeed, all the considerations that will be done are valid for the other constellations too.
As illustrated in Fig. 1.2, GPS signals are transmitted over frequencies $f_{L1} = 1575.42$ MHz and $f_{L2} = 1227.60$ MHz. Both frequencies are derived from a common value of 10.23 MHz, generated by the atomic clocks on board the satellites, to allow maintaining synchronization. Additionally, the rates of the code and of the navigation data are derived from this value.
On frequency L1, two signals are transmitted. One can be used by civil users while the other is reserved for Department of Defence (DoD)-authorized users only. As for L2, only one signal for DoD-authorized users is transmitted. To obtain the two different signals, two ranging codes are used: Precision codes P (denoted with Y code if encrypted) and Coarse/Acquisition (C/A) codes [8]. Both can be combined with navigation data.
The C/A code is quite short, to allow a fast acquisition of the signal, even if not precise. It is made of $p = 1023$ chips and it is characterized by a chip rate of

$R_{chip} = 1.023$ Mchip/s. The chip duration is therefore $T_{chip} = 1/R_{chip} \sim 1$ µs, leading to a total code duration of $T_{code} = p \cdot T_{chip} = 1$ ms. This code is periodic and it is repeated every $T_{code}$. Regarding the navigation data, it has a rate of 50 bits/s, with a bit duration of $T_b = 20$ ms.
P codes instead are very long codes, with a chip duration much smaller than C/A codes, offering a better precision in the range measurements.
Summing up all these components, the SISs transmitted by the antenna of the $k$-th satellite on frequencies L1 and L2 are respectively

$$\begin{aligned} s_{L1}^{(k)}(t) = {} & \sqrt{2P_C} x^{(k)}(t) D^{(k)}(t) cos(2\pi f_{L1} t + \theta_{L1}) \\ & + \sqrt{2P_{Y1}} y^{(k)}(t) D^{(k)}(t) sin(2\pi f_{L1} t + \theta_{L1}) \end{aligned} \tag{1.3}$$

$$s_{L2}^{(k)}(t) = \sqrt{2P_{Y2}} y^{(k)}(t) D^{(k)}(t) sin(2\pi f_{L2} t + \theta_{L2}) \tag{1.4}$$

where $P_C$, $P_{Y1}$ and $P_{Y2}$ are the signal powers of signals corresponding to C/A-code on L1, P(Y)-codes on L1 and L2; $x^{(k)}$ and $y^{(k)}$ are the C/A and P(Y) codes relative to satellite $k$. Whereas, $D^{(k)}$ is the navigation data stream and $\theta_1$ and $\theta_2$ are the carriers phase off-sets [8]. As can be derived from equation 1.3, the C/A code is the quadrature component of the signal and the P-code is the in-phase one.

## 1.3 Receiver architecture

A GNSS receiver is responsible for measuring the propagation time $\tau$ of the signals broadcasted from GNSS satellites, in order to compute its range from these satellites and finally estimate the user location with the highest accuracy and precision. Another important parameter to estimate is the Doppler shift $f_D$, since it contains information about pseudorange rate, which are necessary to compute user velocity and clock drift.
Firstly, GNSS receivers must determine which satellites are visible and which are not. Therefore, these are continuously looking for the presence of radio signals to be acquired and then tracked, so as to correctly extract the information needed to solve the Position, Velocity, Timing (PVT) equations.
Although in GNSS it does not exist a unique receiver architecture, the main blocks used by a generic GNSS are quite standard. First of all, an antenna is capturing the SIS signals emitted by GNSS satellites, together with noise and interference. Considering again a GPS satellite, the received signal is modelled as:

$$r(t) = \sqrt{2P_{RX}} D(t-\tau) x(t-\tau) cos\Big(2\pi(f_L + f_D)t + \theta_{RX}\Big) + w(t) \tag{1.5}$$

where $\tau$ is the code delay given by propagation and $f_D$ is the Doppler shift; $w(t)$ is the noise, modelled as zero mean White Gaussian Noise (WGN) random process.

Of course, the received power $P_{RX}$ is significantly weaker than the transmitted one, due to all the impairments experienced by the signal travelling from the spacecraft to the Earth [8].

Once the signal is received, it goes to the front-end stage, which filters, down-converts, samples and quantizes the signal. Then there are two stages, referred to as acquisition and tracking of the signal performing Digital Signal Processing (DSP). These stages work on independent channels simultaneously. Each channel is dedicated to a specific signal from a specific satellite. For the sake of explanation, from now on only a single channel is considered.

Acquisition is a sort of preliminary step, identifying which satellites are present and starting processing them. Its output is fed to the tracking stage, that is where the delay of the local code replica, used for the pseudorange computation, is actually estimated. Once the pseudorange is computed, the PVT solution can be estimated. Actually, acquisition and tracking run in parallel and in a continuous way on the incoming signals, because satellites appear and disappear over time.

### 1.3.1 Front-end

The incoming RF signal is captured through the receiver antenna and goes to the first stage of the receiver, which is the front-end (see Fig.1.4). This block works with the analogue signal and it is responsible for conditioning the signal, so to preparing it for the following stages performing digital baseband signal processing. Although a standard implementation of the front-end receiver is not defined, the main components of the GNSS front-end are [9]:

- *Filtering and amplification*: a bandpass filter is used to limit the out-of-band interference of the incoming signal and to guarantee low noise. Filtering affects the signal in terms of shaping and noise. The filter is followed by an amplifier used to increase the power of the received signal.
- *Down-conversion*: the down-conversion is made to move the RF spectrum of the signal directly to baseband or, typically, to an Intermediate Frequency (IF) close to it. Starting from the received signal (1.5), the resulting down-converted signal is:

$$r_{IF}(t) = \sqrt{2P_{RX}}D(t-\tau)x(t-\tau)cos\Big(2\pi(f_{IF}+f_D)t+\theta_{RX}\Big)+w(t) \quad (1.6)$$

- *Sampling and Quantization*: the signal is then converted from analogue to digital through an Analogue-to-Digital Conversion (ADC).
- *Automatic Gain Control*: the Automatic Gain Control (AGC) is an adaptive system used to adjust the gain of the front-end in order to take advantage of the full dynamic range.

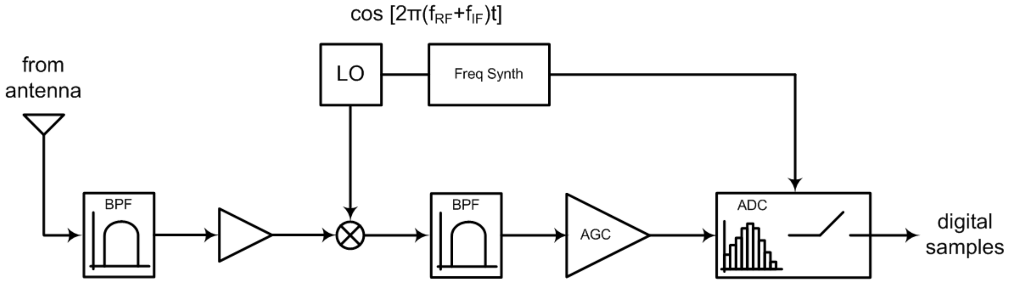

**Figure 1.4:** GNSS receiver front-end. Picture taken from [9]

### Carrier-to-noise ratio

The bandwidth of the front-end filter, $B_{fil}$, fixes the power of the receiver signal. Usually, a bandwidth large enough to avoid filtering useful power is chosen. The value of the Signal-to-noise ratio (SNR), commonly defined as the ratio between the useful signal power and the noise power, at the output of the front-end, depends on the choice of the filter bandwidth:

$$SNR = \frac{C}{N_0}\frac{1}{B_f} \tag{1.7}$$

where $N_0$ is the noise power density and C is the signal power evaluated on the entire signal bandwidth. In GNSS, another quantity, independent from the filter bandwidth, is used to express the ratio between the signal power and the noise power. This quantity is called Carrier-to-Noise density ratio ($C/N_0$) and it is defined as the ratio between the maximum signal power C and $N_0$. This quantity is measured in dB-Hz and it can just be estimated by the receiver, cannot be directly computed.

## 1.4 Acquisition stage

The front-end stage provides as output the discrete-time version of the down-converted received signal (1.6), suitable for digital signal processing. The digital signal, composed by noisy samples $r_{IF}[n]$, is characterized by three unknowns components, which are the code delay $\tau$, the Doppler shift $f_D$ and the carrier phase offset $\theta_{RX}$. Acquisition aims to find a fast and rough estimation of $\tau$ and $f_D$, sufficiently good to initialize the tracking stage and let it start working. The vector of parameters to identify, can be defined as $\mathbf{p} = (\tau, f_D)$. Regarding the carrier phase offset, it is not estimated in this stage.
Since ranging codes are characterized by useful mathematical properties, as already anticipated earlier, the estimation of $\mathbf{p}$ is done by means of correlation operations.

PRN sequences allow the receiver to distinguish signals transmitted by different satellites through correlation operations. In fact, the correlation of any two PRN codes related to different satellites is low [10]. Moreover, each PRN code is also uncorrelated with itself exception made for the zero shift, which means that the auto-correlation function of a PRN code is almost zero unless for zero shift, in which it presents a distinct peak. Therefore, correlation operations can be exploited both to understand if a specific satellite is visible, and to understand which is the delay and the Doppler shift of the received signal. In order to do this, a local code replica must be generated inside the GNSS receiver. In particular, this replica, containing a reproduction of the PRN code and of the carrier, is used as a test signal, meaning that different values of $\bar{\tau}$ and $\bar{f}_D$ are tried until the maximum value of the correlation is found. Hence, what is implemented is the Maximum Likelihood (ML) estimation of $\mathbf{p}$:

$$\hat{\mathbf{p}}_{ML} = arg\max_{\mathbf{p}} \left| \frac{1}{N} \sum_{n=0}^{N-1} r_{IF}[n]\bar{l}_{IF}[n] \right|^2 \tag{1.8}$$

where N is the number of considered samples; $\bar{l}_{IF}[n]$ is the local signal replica, reproducing a local code $c$ with code delay equal to $\bar{\tau}$ and a local carrier generated with a Doppler frequency shift equal to $\bar{f}_D$:

$$\bar{l}_{IF}\left[n\right] = c\left[n - \bar{\tau}\right] e^{j2\pi\left(f_{IF} + \bar{f}_D\right)n} \tag{1.9}$$

Since the carrier phase offset is unknown, a complex exponential must be used in (1.9) in the generation of the local carrier.

### 1.4.1 Cross Ambiguity Function evaluation

In order to estimate the values of $\tau$ and $f_D$, a two-dimensional correlation function between the received signal and the local replica is used, defined as Cross-Ambiguity Function (CAF):

$$Y(\bar{\tau}, \bar{f}_D) = \frac{1}{N} \sum_{n=0}^{N-1} r_{IF}[n]c[n - \bar{\tau}]\ e^{j2\pi(f_{IF} + \bar{f}_D)n} \tag{1.10}$$

Since the carrier phase offset is unknown, and is not estimated in this stage, only the envelope of (1.10) is considered $S(\bar{\tau}, \bar{f}_D) = |Y(\bar{\tau}, \bar{f}_D)|^2$ , to avoid the dependence on the phase. This envelope is evaluated over a grid of points (from now on referred to as bins), where each point is a specific value of $\bar{\tau}$ and $\bar{f}_D$. This set of points defines the domain of this function, called Search Space (SS). The goal of acquisition is to find the best estimation of the Doppler and delay, finding the bin corresponding to specific values of these parameters maximizing the CAF and giving best matching between local replica and received signal. The Search Space is made of $N_\tau \times N_D$ bins. Since the correlation is done between digital samples, both the number of delay and Doppler shift bins to be tested depends on the sampling frequency $f_s = 1/T_s$. Therefore, it is important to choose the sampling frequency in such a way to guarantee a sufficiently good estimation in the acquisition to allow the convergence of the tracking. In particular, the resolution of the delay estimation depends on the number of samples per chip $N_c = T_{chip}/T_s$. The minimum shift between the 2 sequences is 1 sample, therefore it corresponds to the sampling time $T_s$.

The time window taken into account for the computation of the CAF is referred to as coherent integration time $T_{coh} = NT_s$. This window is a multiple of the code period $T_{code}$. The number of delay bins is given by:

$$N_\tau = \frac{T_{coh}}{T_s} = T_{coh} f_s \tag{1.11}$$

The longer the duration of the code, the larger the number of delay bins.

It is worthwhile remarking that the delay is a parameter in time domain, but what is performed is a correlation between the two digital codes. Therefore, what is actually estimated is a code phase, not the delay of the signal coming from the satellite to ground. Due to the periodicity of the incoming code, the correlation peak, corresponding to the best matching between the received code and the local replica, falls within one code period $T_{code}$.

As regards Doppler domain, it is necessary to select a Doppler range $(-\bar{f}_{D,max}, +\bar{f}_{D,max})$ to be analysed, depending on the specific application of the receiver. In fact, contributions such as the user motion and the user clock drift must be taken into account. Once the Doppler range has been established, the number of Doppler frequency bins depends on the choice of the bin size. In this thesis, it has been followed the empirical rule granting a worst case loss below 3 dB, when the actual $f_D$ is not exactly one of the tested values and it falls in the middle of the bin:

$$\Delta f = \frac{2}{3T_{coh}} \tag{1.12}$$

hence, the number of Doppler frequency bins depends on the coherent integration time. A large $T_{coh}$ corresponds to a small Doppler bin, which means more bins to test. Once the domain of the CAF has been defined, correlation operations are performed. For each PRN code, all possible $\bar{\tau}$ and $\bar{f}_D$ are tested, until the correlation peak is found, that is the maximum value of the CAF. If this value exceeds a predefined threshold B, the $\bar{\tau}$ and $\bar{f}_D$ of the local signal are estimated, meaning that they are passed to the tracking stage. Fig. 1.5 shows an example of the plot of the normalized 3-D CAF, referred to the acquisition of a GPS L1 C/A code with $C/N_0 = 45$ dB-Hz. In particular, the y-axis represents the values of the Doppler frequency bins [Hz], while the x-axis the values of the code delay bins [chips] and the z-axis the correspondent values of the correlation function, normalized to the maximum value.

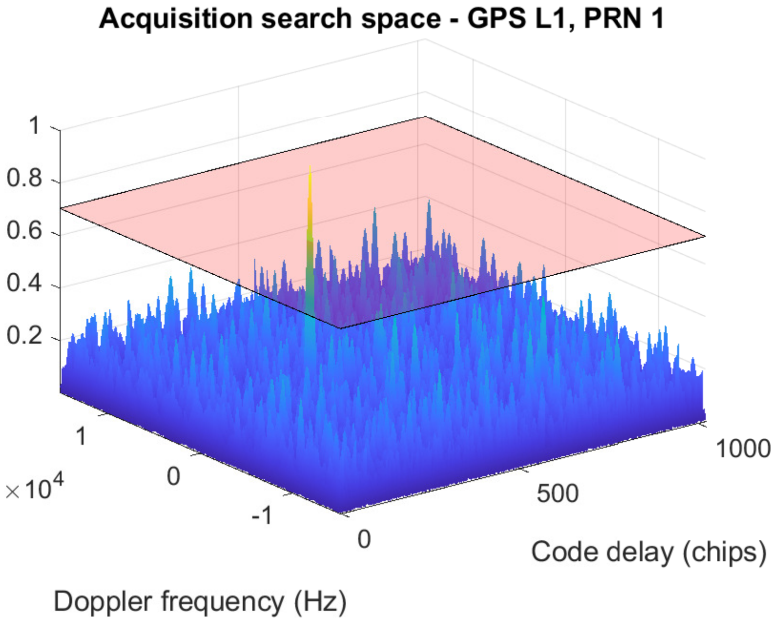

**Figure 1.5:** Example of CAF for a GPS L1 C/A code with $C/N_0 = 45$ dB-Hz

A key parameter to evaluate the performance of a GNSS receiver is the Time To First Fix (TTFF), which is the time needed to acquire satellite signals and get the PVT solution. The acquisition is the main contribution affecting the TTFF, thus it must be as simpler and faster as possible. The time required by the acquisition depends on the time spent to compute the CAF, which depends on the size of the Search Space: the smaller it is, the less time consuming is the acquisition process. However, a smaller SS corresponds to a small probability of catching the right values. Therefore even other techniques are used to minimize the acquisition process. First of all, the approximate time and position of the receiver, together with the almanac data, can be exploited to understand if a specific GNSS spacecraft could possibly have LOS with the receiver itself, in order to decide whether to keep it from the PRN codes to test or remove it. Besides the number of PRN codes to test, it is possible to reduce also the size of the Search Space if external information are available. This acquisition simplification is called *warm/hot start-up* and will be explained better later on in Chapter 2, since it is one of the main points of this work. On the contrary, if no external aids are available to the receiver, the entire SS must be evaluated, for all the ranging codes, and is referred to as a *cold start-up*.

The time needed by the acquisition stage depends also on the complexity of the strategy employed to evaluate the CAF. Below, follows the description of different methods.

### Serial acquisition scheme

In the Serial acquisition scheme, all possible combinations of $\bar{\tau}$ and $\bar{f}_d$ are tested and, at each trial, a single value of the ambiguity function is obtained. The time required for this process is directly proportional to the number of bins to explore. Fig. 1.6 shows the scheme of this method.

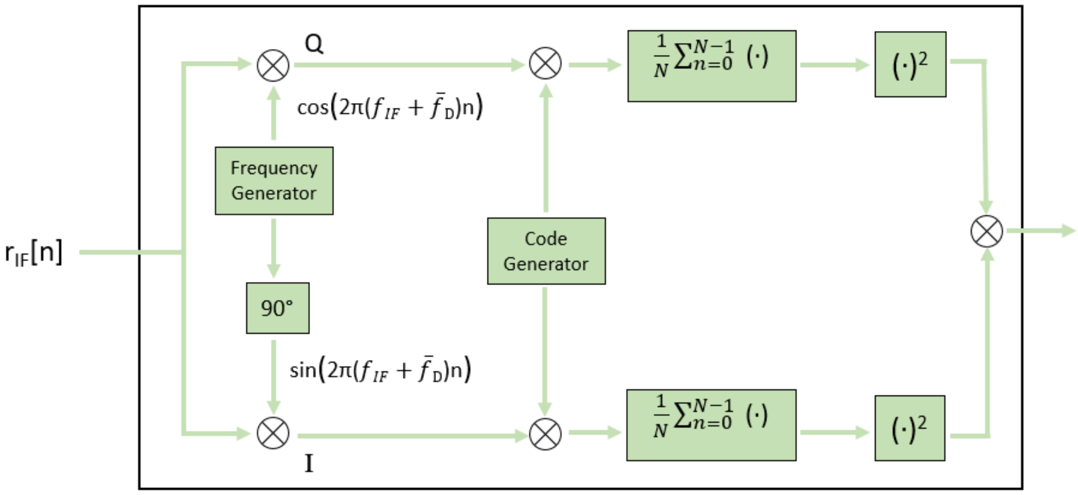

**Figure 1.6:** Serial acquisition - Block scheme

The samples of the received signal are multiplied by two orthogonal sinusoids, generated by the frequency generator, at carrier IF plus the Doppler shift to test. In (1.9), a complex exponential is present and therefore two branches are needed in the serial search scheme, one for the in-phase component and the other for the quadrature one. These multiplications allow the carrier wipe-off, meaning that the signal is no more modulated by the carrier frequency. The two outputs are multiplied by the local code, delayed by the $\bar{\tau}$ to test. Then, the correlation operations are done, obtaining the real and imaginary components of the CAF which are then summed to obtain the final value. Since the noise variance, after the correlation, decreases by a factor of N, the longer is the considered sequence, the less is the noise. However, if N is large, also the coherent integration time is large leading to a smaller frequency bin size, which means more bins to explore. Therefore, the value of N must be chosen carefully, taking into account both noise

averaging and time.
Serial acquisition requires an high number of operations and it is time consuming. To overcome this issues, it can be substituted with a parallel search exploiting the properties of the Discrete Fourier Transform (DFT) operations. In fact, parallel acquisition allows to obtain more values of the ambiguity function simultaneously and it can be implemented in both the domains of the CAF. Which scheme, and so which domain, is better depends on the application and on the desired resolution in the two domains.

### Parallel acquisition in the time domain

Parallel acquisition in time domain is the technique adopted in this thesis work. Differently from the serial scheme, here groups of cells are tested simultaneously, meaning that the entire correlation function, for a given value of $\bar{f}_D$, is obtained at each step. Fig. 1.7 shows the block scheme of this acquisition method.

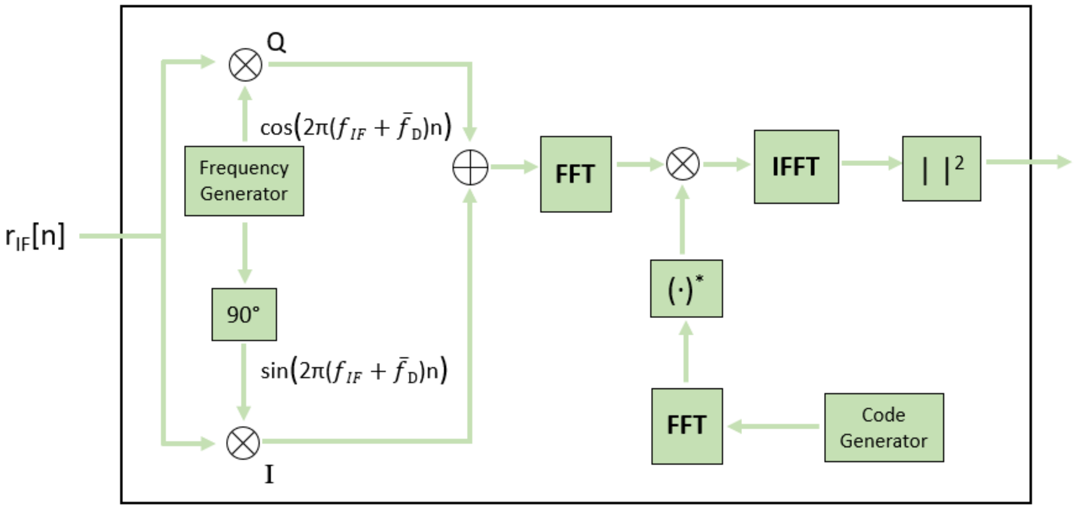

**Figure 1.7:** Parallel acquisition in time domain - Block scheme

From the stream of received samples, N values are collected and multiplied by the two sinusoids. The two outputs, corresponding to the in-phase component and the quadrature one, are summed. Then, the Cross-Correlation Function (CCF) between this sum and the local replica is implemented by means of the circular correlation, obtained through Fast Fourier Transform (FFT) and Inverse Fast Fourier Transform (IFFT) operations:

$$Y(\bar{\tau},\bar{f}_D) = \frac{1}{N} IDFT\Big\{DFT\{r_{IF}[n]e^{j2\pi\left(f_{IF}+\bar{f}_D\right)n}\}DFT\{c[n]\}^*\Big\} \tag{1.13}$$

Finally, the square module is computed and what is obtained is a function of N points, corresponding to the values of the CAF of all the $\bar{\tau}$, for a fixed value of $\bar{f}_D$. The resolution in the frequency domain is chosen arbitrarily, while the resolution in the time domain depends on the number of points of the FFT. As regards the processing time, it is proportional to the number of Doppler f bins to analyse. Usually, $N_D$ is smaller than $N_\tau$, therefore this method turns out to be very efficient.

### Parallel acquisition in the Doppler domain

Parallel acquisition in Doppler frequency domain is the dual implementation of the one in time domain. In this case, for each fixed value of $\bar{\tau}$, all the values of $\bar{f}_D$ are computed simultaneously, with only one FFT calculation.
The incoming signal is multiplied by local code with fixed delay and the FFT of this product is done (Fig. 1.8). In that way, the entire values of the CAF in Doppler domain, are obtained.

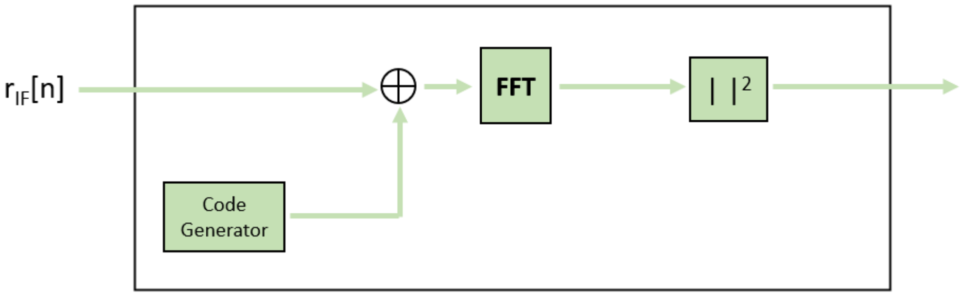

**Figure 1.8:** Parallel acquisition in Doppler domain - Block scheme

In this method, $\Delta f$ cannot be chosen arbitrarily, so there is no freedom in choosing the resolution in frequency. In fact, the resolution in the Doppler domain is:

$$\Delta f = \frac{1}{T_{coh}} \tag{1.14}$$

## 1.4.2 Decision logic

During the evaluation of the CAF, a decision must be taken about whether the satellite is present or not and if it is aligned with the local replica. To do so, different strategies can be adopted. As previously shown, the value of the CAF is obtained through the correlation of the local replica and the received signal. Since the received signal contains noise, which is a stochastic component, the value assumed in each bin of the search space can be represented by random cells $X_n$

with $n = 1,2,..,N$. Hence, to set a threshold $B$ regarding the values of the CAF and to evaluate the performance of the acquisition, the Neyman-Pearson criterion is used. In particular, the null hypothesis $H_0$ is verified when the signal is not present or not aligned with the local replica. Instead, the alternative hypothesis $H_1$ is obtained when the signal is present and correctly aligned. The random cells $X_n$, related to hypothesis $H_0$, are distributed according to [11]:

$$X_n|H_0 \sim f_{X_n}(\beta) \tag{1.15}$$

while the random variable verifying hypothesis $H_1$ is distributed according to:

$$X_n|H_1 \sim f_A(\beta) \tag{1.16}$$

and it is denoted by $X_A$.
Due to the presence of noise, it can happen that the value of a cell exceeds the threshold in the wrong bin, leading to a false alarm. The cell false alarm probability is given by:

$$P_{fa}(B) = \int_B^{+\infty} f_{X_n}(\beta) d\beta \tag{1.17}$$

The detection probability instead, is the probability that the signal is detected in the correct bin and it is given:

$$P_d(B) = \int_B^{+\infty} f_A(\beta) d\beta \tag{1.18}$$

Since system performance strongly depends on the whole search space, not only on the single cell statistics, the acquisition decision is taken based on it. Therefore, it is important to evaluate the overall false alarm probability $P_{FA}$ and the overall detection probability $P_D$. These probabilities depend on the search strategy used to determine the presence of a satellite:

- *Maximum*: the correlation function is evaluated for each value of Doppler shift and code delay, then the decision is taken comparing just the maximum value of the CAF to the threshold $B$.

- *Serial*: the CAF is serially evaluated cell by cell and each value is compared to the threshold. As soon as a value crosses the threshold, the acquisition process stops.

- *Hybrid*: this strategy is usually implemented in acquisition schemes based on the FFT. The ambiguity function is evaluated row-by-row (or column-by-column) and the maximum of each row is compared against the threshold to take the decision.

In this work the *Maximum* strategy has been adopted. Thus, the hypothesis $H_1$ is verified when the maximum value of the correlation function is assumed by $X_A$ and it crosses the threshold $B$. For this strategy, the overall detection probability $P_D$ and the overall false alarm probability $P_{FA}$ are given by:

$$P_D = \int_B^{+\infty} [1 - P_{fa}(\beta)]^{N-1} f_A(\beta) d\beta \tag{1.19}$$

$$P_{FA} = 1 - \Big(1 - P_{fa}(B)\Big)^N \tag{1.20}$$

Inverting Eq. (1.20), the cell false alarm probability, depending on the whole search space, is obtained. Finally, it can be demonstrated [12] that the cell false alarm probability is equal to:

$$P_{fa}(B) = exp\Big( - \frac{B}{2\sigma^2}\Big) \tag{1.21}$$

where $\sigma^2$ is a parameter related to the input useful signal amplitude and noise variance $\sigma^2 = \frac{\sigma_{IF}^2}{2} H$. Therefore, once we evaluate the cell false alarm probability $P_{fa}$ from Eq. (1.20), the threshold B can be fixed according to Eq. (1.21).

## 1.5 Tracking stage

Acquisition provides a first and approximate estimation of the delay and Doppler parameters $\hat{\mathbf{p}}^{(a)} = \Big(\hat{\tau}^{(a)}, \hat{f}_D^{(a)}\Big)$. This estimation is given to the tracking stage, which is in charge of refining and following continuously these values in order to keep the alignment between the received code and the local replica. To reach its objective, for each channel, tracking exploits a double feedback loop structure composed by the Phase-Locked Loop (PLL) and the Delay-Locked Loop (DLL), as shown in Fig .1.9. The scheme works in an iterative way and it is initialized by the output of the acquisition. In particular, $\hat{\tau}^{(a)}$ is fed to the local code generator, while $\hat{f}_D^{(a)}$ is fed to the local carrier generator. The received signal $r_{IF}[n]$ is split into two branches, one of them is multiplied by the local code and the other by the local carrier, obtaining a code wipe-off and a carrier wipe-off respectively. The results of these operations are a clean sinusoid and a clean code. The first one is injected into the PLL, which implements the carrier tracking, getting at each iteration a better estimation of the Doppler frequency. Conversely, the other is exploited by the DLL, which works on the baseband signal realizing the code tracking to keep the two codes aligned. Being an iterative process, the refined estimations of $\tau$ and $f_D$ will once again be fed to the code and frequency generators.

The tracking is said to be locked when a stable solution for the double loop is found. If the parameters estimated by acquisition are good enough, tracking

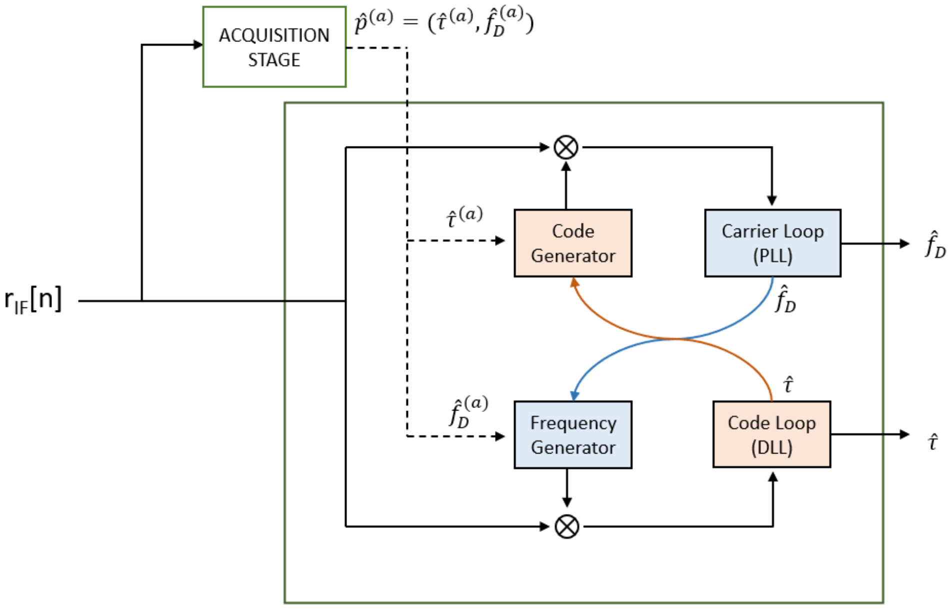

**Figure 1.9:** Tracking stage - Block scheme

converges to best estimation of delay and Doppler. These values are the actual estimation that allows to construct the pseudorange, that is why this stage is the core part of the GNSS receiver. In fact, since a bias in the tracking loop generates a bias in the pseudorange measurement, the quality of the pseudorange is strictly dependent on the quality of the tracking.

In the scheme just described, where DLL works jointly with the PLL, a full demodulation of the signal is done, exploiting a signal which is coherent, both in frequency and in phase, with the incoming signal. This implementation is called coherent DLL. However, DLL can work also without the recovery of the phase offset. This version is therefore called non-coherent DLL. The carrier wipe-off is still implemented, using a Frequency-Lock Loop (FLL) as carrier removal, but with an uncertainty on the phase. FLL is faster with respect to PLL and it should be used in high dynamics applications.

## 1.6 Pseudorange construction and PVT solution

Once the tracking finds the best estimation of delay, Doppler shift and, eventually, phase offset, it is then possible to measure the propagation time. This value can be computed as the difference between the signal reception time, measured in the receiver time-scale, and the signal transmission time, which is instead measured in the GNSS time-scale. In order to retrieve the latter information, the demodulation of data, is required and to correctly extract the data message, a perfect synchronization between the received signal and the local replica is needed. Once the apparent transit time is computed, multiplying it by the speed of light, the pseudorange is obtained. However, as already shown in Eq. (1.2), this pseudorange contains a bias, due to the misalignment between the user clock and the GNSS time-scale. Hence, as anticipated earlier, at least four pseudorange measurements are necessary, since there are four unknowns to be retrieved, which are the coordinates of user location $(x_u, y_u, z_u)$ and the user clock bias $\delta t_u$.

Another important information that can be recovered from the navigation data is the satellites velocity vectors, which, together with the pseudorange rates (evaluated through estimated Doppler frequency) can be used to compute the user velocity [8].

After computing the pseudoranges and the pseudorange rates, it is possible to obtain the PVT estimation through mathematical methods, such us the Least-Squares (LS) and Weighted-Least-Squares (WLS) approaches. Anyway, this thesis work does not deal with the pseudorange construction. A more detailed description can be found in [13].

Concerning the quality of the PVT estimate, it depends on different factors. Firstly, the more satellites are used to make computations the better is the estimation. Besides the number of satellites in view, plays an important role the satellite geometry, which is the spatial distribution of the satellites in the sky, relative to the user. A good geometry corresponds to satellites spread in all directions, some of them high and the others low. On the contrary, when satellites are aligned the accuracy of the estimation is worse.

# Chapter 2

# Use of GNSS in space

## 2.1 State-of-the-art GNSS receivers for space applications

GNSS has been originally designed to provide accurate Positioning, Navigation and Timing (PNT) information to terrestrial users. However, these navigation systems are now increasingly exploited for autonomous space navigation as well. In particular, GNSS receivers in space have been already validated in low orbits, such as in LEO, since early 2000s. The use of in-orbit GNSS-based systems is becoming attractive even for spacecraft navigation at higher altitudes, for example, in lunar missions.

In *The Interoperable Global Navigation Satellite Systems Space Service Volume* booklet, of the United Nations, the performances of using GNSS signals at high altitude have been analysed. In this booklet [14], the Space Service Volume (SSV) is defined as the area between 3,000 km and 36,000 km above the surface of the Earth. Based on different characteristics, in terms of geometry and signal availability, the SSV is further subdivided into 2 regions: the Lower SSV for medium Earth orbits and the Upper SSV for geostationary and high Earth orbits (Fig. 2.1). The lower SSV covers altitudes from 3,000 km to 8,000 km, while the upper SSV from 8,000 km to 36,000 km, which corresponds to the Geostationary-Earth Orbit (GEO).

In the lower SSV, satellites orbit lower than GNSS constellations and therefore they are able to receive GNSS signals both from the spacecraft nadir and zenith direction with respect to the Earth. On the contrary, in the upper SSV, satellites orbiting at altitudes above the GNSS constellations are not able to receive GNSS signals from the spacecraft zenith direction. Indeed, signals are received only from nadir-pointing antennas, which means they arrive from the opposite side of the Earth, resulting in reduced received power and poorer availability. In order to improve the number of visible satellites in the upper SSV, an interoperable GNSS SSV should be used, where GNSS signals from different constellations are exploited simultaneously. Additionally, using a proper antenna and adequate signal processing techniques (shown in Sec. 2.2), would improve the processing of weak GNSS signals in these conditions.

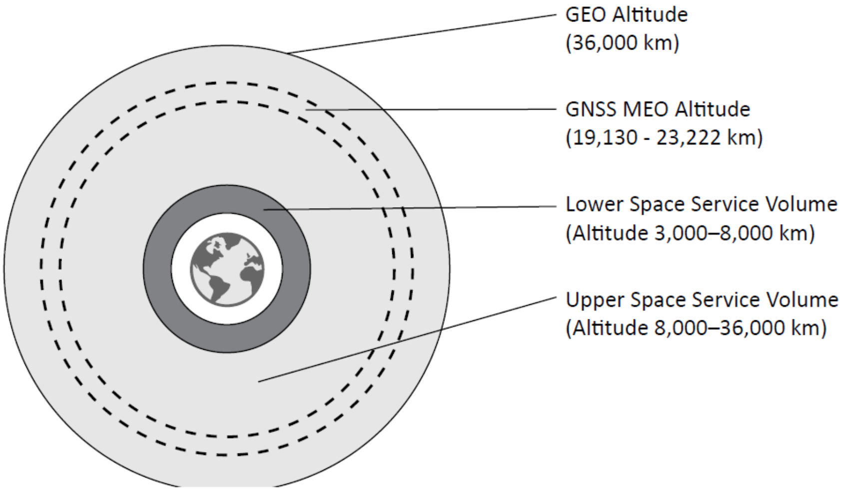

**Figure 2.1:** GNSS Space Service Volume. Picture taken from [14].

The interest in expanding the use of autonomous space navigation at higher altitudes significantly grew. In fact, it would give many benefits for space missions, like reliability, spacecraft autonomy, cost reduction and improvement in accuracy. Over the past decades, space missions have leveraged mainly on Precise Orbit Determination (POD), which is the process of accurately estimating and tracking both position and velocity of spacecraft along the orbit. This method usually relies on post-processing computation, based on range and Doppler tracking services offered by the ground segment. In order to frequently provide spacecraft with updates of these information, a communication link with a global network of ground stations is utilized. For example, these tracking services are offered by NASA Deep Space Network (DSN) and the European Space Tracking Estrack network, composed by very huge and accurate antennas. In particular, position and velocity of satellite are estimated through radiometric measurements like range data, Doppler measurements and Very Long Baseline Interferometry (VLBI). The latter is a technique which provides a measure of the spacecraft angular position, sometimes resulting even more accurate than the one determined using Doppler and range data [15]. These techniques, exploiting ground computations, allow to obtain good accuracy. Nevertheless, since the spacecraft cannot navigate autonomously and it has to always rely on the ground segment, these techniques are very expensive and not scalable to a large number of missions. On the contrary, the use of real-time, in-orbit GNSS-based navigation systems would make the spacecraft more autonomous, reducing the costs and the effort of ground operations. However, using GNSS receivers at high altitudes, above the GNSS constellation, is a challenging task due to multiple factors:

- *Low signal power levels*: due to the long distance and the occultation of the Earth, the received GNSS signals are characterized by low power levels. As shown in Fig. 2.2, only a small part of the signals transmitted from GNSS satellite's main antenna lobe is received from GNSS receivers, orbiting on the opposite side of the Earth. Therefore, side lobes play a significant role in these conditions, but they only provide low-power signals in the spacecraft direction.

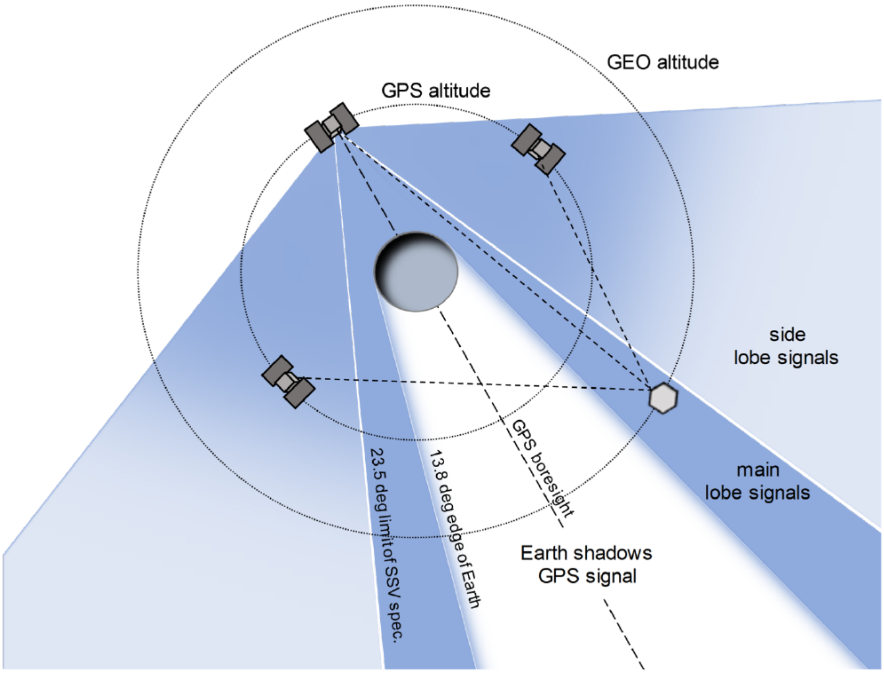

**Figure 2.2:** GNSS transmit antenna lobes. Picture taken from [16].

- *Reduced satellite visibility and poor geometry*: at these altitudes, the satellite visibility is drastically reduced, leading to a poor geometric diversity and therefore to a worse precision of the positioning and navigation solutions.
- *High dynamics*: GNSS space-born receivers could experience high relative dynamics with respect to the GNSS satellites, which are responsible for high values of both Doppler frequency and Doppler rate. In order to be able to

correctly perform acquisition and tracking operations, Doppler frequency must be estimated and compensated for, as will be explained better in Chapter 3.

Recent research studies shown the feasibility of exploiting the use of Earth GNSS signals at higher altitudes, such as in Moon Transfer Orbit (MTO) and lunar orbits [17]. Therefore, there is an interest in extending the definition of the SSV above GEO, till the Moon. More details about the use of GNSS for lunar missions will be given in Chapter 4.

## 2.2 Techniques for weak GNSS signals acquisition

In harsh environments, as it is space, the GNSS signal is subjected to more severe distortions, leading to a smaller $C/N_0$ with respect to the levels experienced in clear sky and therefore to lower quality of the estimated position. In these scenarios, high sensitivity GNSS receivers must be employed. These receivers exploit signal processing techniques allowing to increase the robustness of the receiver to low signal-to-noise ratio, especially in the acquisition stage. In fact, in section 1.4, it has been explained that the main task of the acquisition stage is to find the maximum value of the CAF, corresponding to best estimation of the code delay $\bar{\tau}$ and the Doppler shift $\bar{f}_D$. In order to find these values, the correlation peak must emerge from the noise floor. The higher and the sharper the peak, the better is the initialization of the tracking stage, leading to better performance of the receiver. However, the noise samples, $w[n]$, affect each cell of the Search Space and alter the acquisition result. Since this noise is modelled as zero mean Additive White Gaussian Noise, to limit this effect is possible to exploit averaging operations. Noise averaging can be obtained increasing the coherent integration time, which means increasing the number of incoming samples used for the evaluation of the ambiguity function. This averaging can be done before or after taking the envelope of CAF (1.10), corresponding to coherent integration and non-coherent integration time extension respectively.
To facilitate the acquisition stage, it is fundamental also the use of GNSS assistance data, such as estimated Doppler shift and Doppler rate. This thesis focused on strategies and assistance data that improve the acquisition stage.

### 2.2.1 Coherent integration time extension

In coherent integration, the averaging is performed before taking the envelope of the CAF. This strategy is based on increasing the considered samples of the incoming signal from $N$ to $MN$. Since increasing the number of samples corresponds to increase $T_{coh}$, the resulting integration time is equal to:

$$T_{coh} = M \cdot NT_s \tag{2.1}$$

where $M$ is the number of coherent sums and $T_s = 1/f_s$ is the sampling time. The correspondent expression of the CAF is:

$$\begin{aligned} S(\bar{\tau}, \bar{f}_D) &= \left| \frac{1}{M} \sum_{m=1}^{M} \left( \frac{1}{N} \sum_{n=0}^{N-1} r_{IF}[n] c[n-\bar{\tau}] \; e^{j2\pi(f_{IF}+\bar{f}_D)n} \right) \right|^2 \\ &= \left| \frac{1}{MN} \sum_{n=0}^{MN-1} \sum_{n=0}^{N-1} r_{IF}[n] c[n-\bar{\tau}] \; e^{j2\pi(f_{IF}+\bar{f}_D)n} \right|^2 \end{aligned} \tag{2.2}$$

Performing this operation grants an increase of the signal power by a factor proportional to the number of coherent sums $M$. Instead, the noise power is constant, as long as it is zero mean white Gaussian noise [18]. Hence, the SNR after correlation is increased by a factor of $M$. For example, doubling the number of samples $M = 2$ corresponds to an increase of about 3 dB of the SNR. Therefore, after coherent integration time extension the correlation peak will better emerge from the noise floor. Fig. 2.3 shows the plot of the 3-D CAF of a GPS L1 C/A signal, characterized by a $C/N_0$ equal to 30 dB-Hz, for different cases. In the first one (Fig.2.3a), $T_{coh} = 1$ ms has been used in the acquisition stage. While, in the second (Fig.2.3b) the integration time has been extended to 20 ms, which corresponds to performing $M = 20$ coherent sums. Extending the coherent integration time, the peak emerges from the noise floor, exceeds the threshold and it is possible to correctly acquire the signal. On the contrary, using $T_{coh} = 1$ ms, only noise is visible and the signal is not detected.
Increasing the coherent integration time, the resolution in the Doppler domain is increased too. The time needed to evaluate the entire CAF increases as the number of bins increases. Therefore, this technique provides better performance but at the cost of being more timing consuming and more complex. Moreover, there are some issues in extending the coherent integration time, as will be explained in Section 2.2.4. To overcome these limits, non-coherent accumulations can be employed.

### 2.2.2 Non-coherent integration time extension

Differently from coherent combination, in the non-coherent one the averaging operation is done after the envelope of the CAF (1.10). This technique consists in summing K instances of the basic ambiguity function. The squared-envelope removes the dependence on the phase, therefore the CAFs are summed non-coherently [18]. The samples are combined as:

$$S(\bar{\tau}, \bar{f}_D) = \frac{1}{K} \sum_{k=1}^{K} \left| \frac{1}{N} \sum_{n=0}^{N-1} r_{IF}[n] c[n-\bar{\tau}] \; e^{j2\pi(f_{IF}+\bar{f}_D)n} \right|^2 \tag{2.3}$$

Performing this accumulation, both the signal and the noise power increase, but the latter increases less, due to the fact that noise samples are un-correlated. Indeed, the signal power increase by a factor proportional to K, while the noise power increases by a factor $\sqrt{K}$ [19]. Therefore, the gain in noise reduction is lower with respect to the value that would be obtained with the coherent accumulation. This is referred to as squaring loss and makes the non-coherent combination less effective than the coherent one. Anyway, even non-coherent accumulation allows to increase the separation between correlation peak and noise floor.
Since coherent integration is more efficient that non-coherent, in terms on SNR, but it is limited by several factors, a good solution is combining coherent and non-coherent accumulations. The resulting CAF is equal to:

$$S(\bar{\tau}, \bar{f}_D) = \frac{1}{K}\sum_{k=1}^{K}\left|\frac{1}{M}\sum_{m=1}^{M}\left(\frac{1}{N}\sum_{n=0}^{N-1} r_{IF}[n]c[n-\bar{\tau}]\ e^{j2\pi(f_{IF}+\bar{f}_D)n}\right)\right|^2 \tag{2.4}$$

Exploiting both coherent and non-coherent integrations the overall integration time is equal to:

$$T_{ncoh} = K \cdot T_{coh} = K \cdot M \cdot NT_s \tag{2.5}$$

Fig. 2.3c shows the plot of the 3-D CAF of a GPS L1 C/A signal, characterized by a $C/N_0$ equal to 30 dB-Hz, in the case in which $M = 20$ coherent sums and $K = 4$ non-coherent sums have been performed. Combining coherent and non-coherent accumulations allow to obtain good performance in the acquisition stage. In fact, with respect to the case in which only coherent sums are exploited (Fig. 2.3b), the peak is sharper and it emerges more clearly from the noise floor, which is lower compared to the other case. The best trade-off, between number of coherent M and non-coherent sums K must be found depending on the scenario.

### 2.2.3 Differential combination

Another technique, even if not so popular, is the differential combination and it is basically an extension of the non-coherent integration. The complex correlation output is multiplied by the conjugate of the correlation output obtained at the previous integration interval [18]. The resulting function is accumulated and finally the envelope is computed. Indicating with $R[l]$ the output of the correlator at a generic epoch $l$, the CAF becomes:

$$S(\bar{\tau}, \bar{f}_D) = \left|\sum_{l=2}^{L} R[l]R^*[l-1]\right|^2 \tag{2.6}$$

Since the signal samples are highly correlated between consecutive intervals, and instead noise samples tend to be un-correlated, this strategy gives an improvement with respect to the non-coherent one. However, performances are still better in the coherent integration technique.

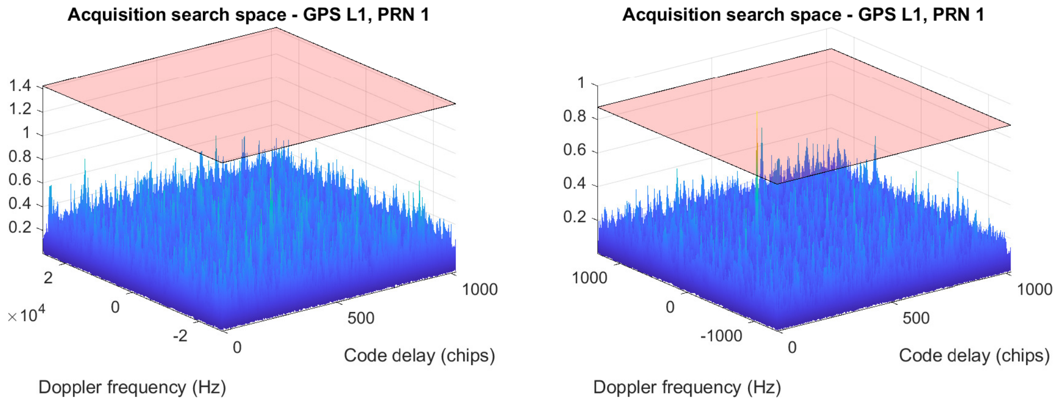

**(a)** $T_{coh}$ = 1 ms, M = 1 coherent sums, K = 1 non-coherent sums.

**(b)** $T_{coh}$ = 20 ms, M = 20 coherent sums, K = 1 non-coherent sums.

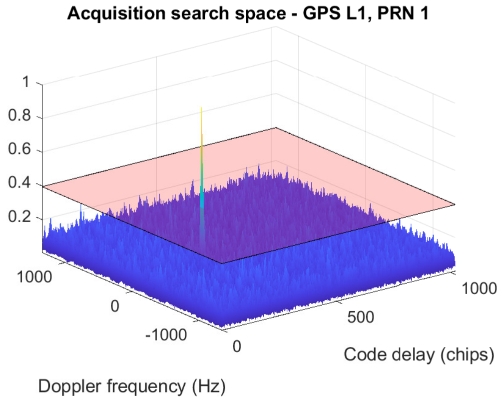

**(c)** $T_{coh}$ = 20 ms, M = 20 coherent sums, K = 4 non-coherent sums.

**Figure 2.3:** Acquisition of a GPS L1 C/A signal with $C/N_0 = 30$ dB-Hz. Plot of the normalized 3-D CAF.

### 2.2.4 Limits of integration time extension

The extension of the integration time grants an improve of the receiver performance in terms of sensitivity. However, by extending this interval of time produces some undesired effects, thus, there is a limit on its length.
As shown previously, the majority of GNSS signals are modulated by a navigation message containing useful information about the satellite. The information message contains data-bit transitions, which correspond to a phase shift of 180° in the ranging code. This can generate opposite signs of consecutive correlation blocks, meaning that their coherent accumulation leads to a loss of the correlation peak

[20]. Hence, if no external-aiding giving information about transitions are provided, the extension of the coherent integration time is typically limited to the duration of one bit $T_{coh} \leq T_b$. Considering GPS L1 C/A signals, in this scenario the maximum $T_{coh}$ corresponds to 20 ms.
Figures 2.4 and 2.5 show two examples of the acquisition stage, considering a GPS L1 C/A signal. The navigation message bits, the received code and the local one are indicated, respectively, in green, blue, and red [18]. In both the examples $T_{coh} = 10$ ms. However, in the former there is no data bit transition within the integration interval, since the 10 ms are included in the same bit of the navigation message. In fact, the CAF is characterized by an high and clear peak. Instead, in the second example, the bit transition occurs right at half the integration period. This is the worst case scenario because it leads to an annihilation of the correlation peak.

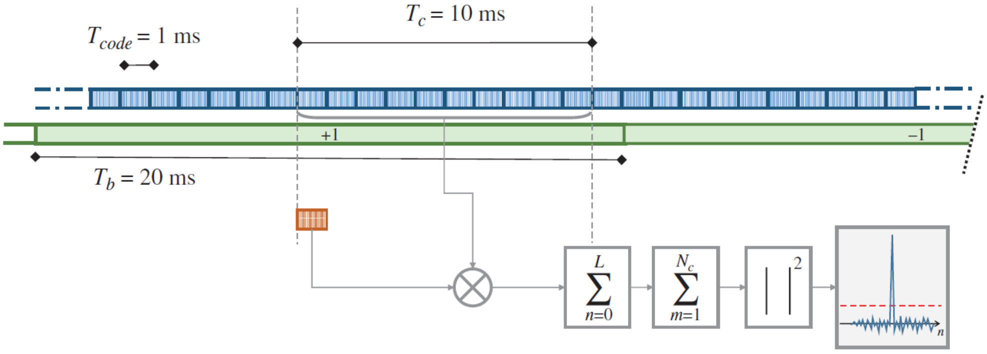

**Figure 2.4:** Acquisition of a GPS C/A signal in the case $T_{coh} = 10$ ms. Picture taken from [18]

When external aids are present, the coherent integration time limitation is neglected and the $T_{coh}$ can be larger than $T_b$. This can be done also when data-less signals are processed, namely pilot channels.
However, the extension of $T_{coh}$ is traded-off with other factors too. Extending $T_{coh}$, the search-space size increases, as well as the computational complexity and the required time in the acquisition process. Therefore, a trade-off between performance and complexity must be found.
The instability of the receiver clock make the acquisition stage harder, especially if $T_{coh}$ is very long, since the carrier and code Doppler effects are more relevant (as it will be deepened in Chapter 3).

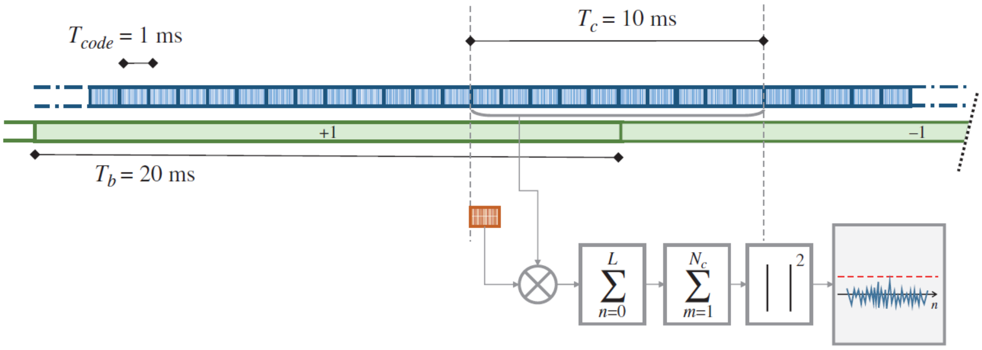

**Figure 2.5:** Acquisition of a GPS C/A signal in the case $T_{coh} = 10$ ms with a bit transition occurring within the integration period. Picture taken from [18]

### 2.2.5 Orbital filter and frequency aiding

Assistance information are essential to facilitate and speed up the receiver operations. Focusing on GNSS space-born receivers, they could experience high relative dynamics with respect to the GNSS satellites, leading to Doppler frequency and Doppler rate values higher than the ones experienced on the Earth surface. Therefore, in these scenario it is of fundamental importance to have some a-priori estimates of these values. These estimates permit to reduce the frequency search space dimension and to extend the integration time in the acquisition stage, allowing the acquisition of signal characterized by very low $C/N_0$. For this purpose, an adaptive Orbital Filter (OF) is exploited to both aid the acquisition and tracking of weak signals and to improve the accuracy in the positioning and navigation solutions, drastically reduced due to the poor geometry and large ranging errors. In [21] an example of implementation of a GPS-based orbital filter for lunar missions is shown in detail, together with its performance. The orbital filter is based on an adaptive Extended Kalman Filter (EKF) and propagates the kinematic state of the spacecraft on its way to the Moon, through the MTO. There are three orbital propagation models taking into account gravity perturbations, based on the altitude of the receivers. Optionally, external sensors could be integrated too. To prevent the orbital propagation solution to drift, it is combined with GPS measurements (pseudoranges and pesuodoranges rates). The Doppler and Doppler rate, given as output by the orbital filter are then fed back to the GNSS receiver, which exploit them during the acquisition and tracking stages. The rate at which these values can be provided to the GNSS signal processing engine depends on how often the orbital filter is iterated by the processor on board the receiver.

The results of this study shown that using an orbital filter as aiding to the acquisition and tracking stage provides a big advantage. It improves the GNSS receiver sensitivity, when weak signals must be processed and few satellites are visible. The receiver robustness against high dynamics is enhanced too. Other studies have demonstrated the importance of using an OF and the benefits it provides in the acquisition and tracking performance [22], [23], [24], [25].

The Doppler and Doppler rate estimation errors depends on the orbital filter accuracy. To correctly perform the acquisition and tracking stages, it is fundamental that the error of these estimations is not too high. In Chapter 4, some considerations about the maximum Doppler aiding error, generated by the Orbital Filter, will be shown.

# Chapter 3

# Impact of the Doppler frequency on the acquisition

Users receiving signals from GNSS satellites observe a Doppler frequency generated by the combination of different factors [18]:

- relative dynamics experienced by the GNSS receiver with respect to GNSS satellites
- the uncompensated frequency offset of the receiver reference oscillator

This Doppler translates in a shift between the transmitting frequency of the satellite and the receiving frequency of the GNSS terminal.

The values assumed by the Doppler frequency and the Doppler frequency rate depend on the considered application. In [26], an analysis about Doppler frequency characterization for GNSS receivers has been carried out in different scenarios. Some of them are taken into account in order to show possible values of the Doppler frequency and the Doppler frequency rate:

- Stationary GNSS Receiver on the Earth surface
- Low-speed GNSS Receiver on the Earth surface
- Low Earth Orbit (LEO) space-borne GNSS Receiver
- Medium Earth Orbit (MEO) space-borne GNSS Receiver

The static user on the surface of the Earth observes small values of both the Doppler frequency and the Doppler frequency rate. In fact, the maximum Doppler frequency shift is about 5 kHz, while the maximum Doppler frequency rate is about 0.93 Hz/s. When instead the receiver is moving, again on the surface of the Earth,

the maximum Doppler frequency linearly increases as the speed of the receiver. Considering for example a speed of 200 km/h, the correspondent Doppler frequency rate is almost 1 Hz/s. Therefore, regardless of whether the user is moving or not, these values are still under control, especially the Doppler frequency rate, meaning that it does not have a great impact on the acquisition stage.
In the simulation regarding a LEO space-borne GNSS receiver, both the Doppler frequency and the Doppler frequency rate assume high values, due to the high speed of space vehicles. Considering the Newton's law of gravitation, the square of the velocity is inversely proportional to the radius of the orbit. Thus, the higher the orbital altitude, the smaller the receiver's velocity and therefore the smaller the Doppler frequency [26]. As shown in Fig. 3.1a, when the GNSS receiver is at an altitude of about 400 km, the maximum Doppler shift is 45.5 kHz, while the Doppler shift rate (Fig. 3.1b) reaches a maximum of about 80 Hz/s for $\theta = 90°$. The angle $\theta$ is linked to the elevation angle of the GNSS satellite as:

$$\mathrm{El} = \begin{cases} \theta - \alpha & 0° \leq \theta \leq 90° \\ (180° - \theta) - \alpha & 90° < \theta \leq 180° \end{cases}$$

where, $\alpha$ corresponds to the angle between satellite-receiver vector and satellite-Earth's origin vector, referenced to a Earth-Centered Earth-Fixed (ECEF) coordinate frame.

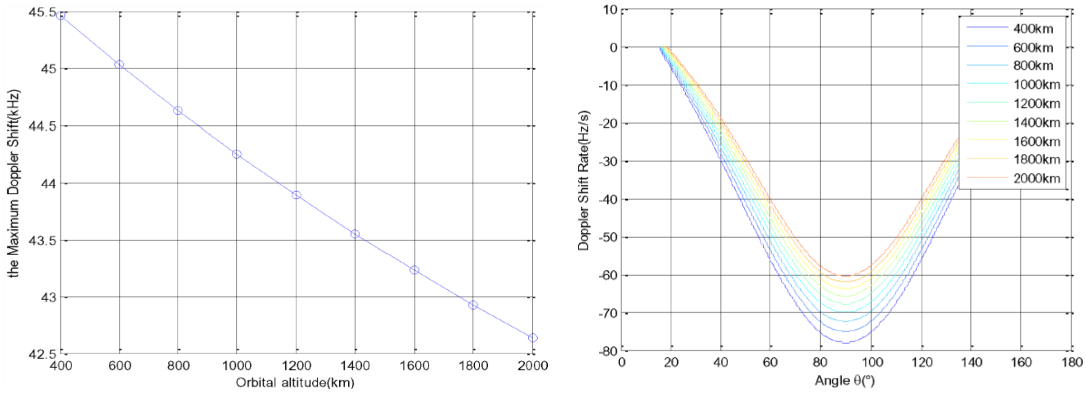

**(a)** Maximum Doppler frequency shift in LEO **(b)** Received Doppler shift rate in LEO

**Figure 3.1:** LEO Space-borne GNSS Receiver Doppler frequency characterization. Plots taken from [26].

Another interesting scenario is MEO space-borne GNSS receiver, where the maximum Doppler frequency shift is approximately a quadratic function of the altitude of the orbit, as shown in Fig. 3.2a. Concerning the Doppler shift rate, it reaches 1800 Hz/s for $\theta = 90°$, when the orbital altitude of the GNSS receiver is almost 20,000 km, since the altitude of GNSS satellites orbits is near 20,000 km. In fact, even if the GNSS receiver's velocity decreases as its altitude increases, the closest the GNSS receiver is to the GNSS satellite, the higher is the Doppler frequency.

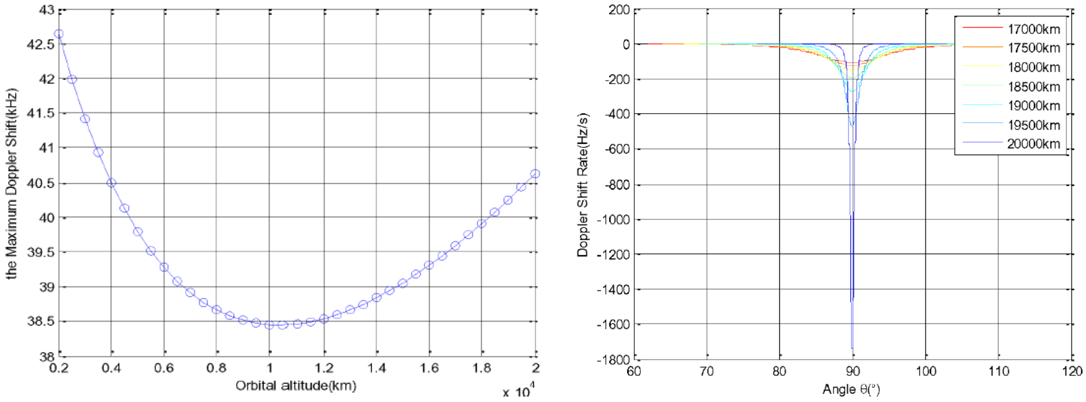

**(a)** Maximum Doppler frequency shift **(b)** Received Doppler shift rate

**Figure 3.2:** MEO Space-borne GNSS Receiver Doppler frequency characterization. Plots taken from [26].

The results just presented show the high values of Doppler frequency for GNSS receivers in space. The Doppler frequency shift and the Doppler frequency rate, have an impact both on the central frequency and on the code frequency. The first is identified as *carrier Doppler*, while the latter is the *code Doppler*. Besides the high dynamic, space-borne GNSS receivers at altitudes above the GNSS constellation, are characterized by very weak signals reception as well. As seen in Sec. 2.2, in these scenarios, high sensitivity signal processing techniques are needed, involving the extension of the integration time. However, increasing the integration time, the negative effects of the Doppler on the signal are more evident. Therefore, in order to properly acquire the signal and tracking it, it is necessary to obtain approximate values of the Doppler shift and Doppler rate and compensate for them.

In the next sections an explanation follows of both the carrier Doppler and the code Doppler. Moreover, an implementation of a compensation of these effects is shown, considering a GPS L1 signal with C/A code, whose detail have been shown in Sec. 1.2.2.

## 3.1 Carrier Doppler

As anticipated earlier, there is a Doppler shift between the transmitting frequency of the GNSS satellite and the GNSS user's receiving frequency, which continuously changes over time. This shift is caused by the relative speed between the transmitter and the receiver, and it is equal to:

$$f_D = \frac{v}{c} f_{L1} \tag{3.1}$$

where $c$ is the speed of light and $v$ denotes the relative velocity between the GNSS satellite and the GNSS receiver in the direction satellite-receiver (i.e. LOS direction).
The acquisition stage takes as input the down-converted and digitalized signal $r_{IF}[n]$. Due to the Doppler offset, the resulting carrier frequency of this signal corresponds to:

$$f_c = f_{IF} + f_D \tag{3.2}$$

The shift $f_D$ from the Intermediate Frequency must be taken into account when demodulating the signal.
In space applications, relative motion between GNSS satellites and GNSS receivers can be very high, leading to high values of Doppler frequency. This scenario, is characterized by weak signal acquisition requiring large integration time. In order to extend the integration time, the Doppler frequency shift, and especially the Doppler frequency rate, must be estimated and compensated for.

### 3.1.1 Carrier Doppler compensation

During the acquisition stage, a carrier wipe-off is done to obtain only the spreading code, suitable for correlation, as explained in Sec. 1.4. To compensate the Doppler frequency shift, the complex sinusoid exploited for the demodulation is characterized by a frequency equal to (3.2). However, the value of $f_D$ is not known, thus, a set of values $N_D$ are tested until the maximum of the correlation operation is found.
The high dynamics of GNSS receivers in space lead to a very large range of Doppler frequency shift values, which means that an high number of Doppler bin must be tested. To overcome this issue, an hint on the possible value of the Doppler frequency must be provide to the GNSS receiver, as seen in Section 2.2.5. Given an estimate of this value, the Doppler frequency domain of the Search Space (SS) can be chosen accordingly. Specifically, the Doppler frequency range is centred on the estimate of the Doppler frequency.

### Doppler rate and linear chirp

The Doppler frequency continuously changes over time, so demodulating the signal considering only a single value of the frequency offset is not sufficient, especially if the shift change occurs very quickly. In fact, the Doppler frequency rate causes the correlation peak to drift from cell to cell. Hence, what comes out from the correlation is a linear chirp which follows the change of the Doppler frequency. A linear chirp is a signal having an instantaneous frequency which linearly varies with time:

$$f(t) = rt + f_0 \tag{3.3}$$

where $f_0$ is the starting frequency, at time $t_0$, and $r$ is the chirp rate. In particular, the instantaneous frequency of the chirp generated in the correlation process goes from the initial value of the Doppler frequency $f_{D,0}$ to $f_{D,0} + (R_D \cdot T_{coh})$, where $R_D$ is the Doppler frequency rate. Therefore, the length of this chirp depends both on the Doppler frequency rate of the signal $R_D$ and on the length of the integration time interval $T_{coh}$. In fact, the larger the integration time and the Doppler frequency rate, the more evident is this effect.

In order to show this phenomena, the results concerning a MEO space-born GNSS receiver, shown in the introduction of this Chapter, are considered. Hence, according to Fig. 3.2, a signal with initial Doppler frequency equal to $f_{D,0} = 40$ kHz and Doppler frequency rate fixed to $R_D = 1800$ Hz/s has been generated and processed with a software GNSS receiver.

Two examples are presented, characterized by two different values of integration time in the acquisition stage. In the first one, an integration time equal to 1 ms, that is the length of one C/A code period, has been used.

Assuming that the receiver is provided with an estimation of the Doppler frequency, the search space can be reduced and centred around this value, implementing a so called *warm start-up*. In order to acquire the generated signal, a parallel acquisition in the time domain has been exploited. Fig. 3.3 shows the 3-D plot of the resulting CAF. Since it has been assumed that an aid on the Doppler frequency is available, the Doppler frequency domain of the search space has been shift around this value. Therefore, in the plot, 0 Hz corresponds to the initial value of the Doppler frequency, that is $f_{D,0} = 40$ kHz. The overall frequency offset is equal to the product between the Doppler rate and the coherent integration interval, that in this case corresponds to $R_D \cdot T_{coh} = 1800$ Hz/s $\cdot$ 1 ms $= 1.8$ Hz. The Doppler step, that is the length of the Doppler frequency bin, is equal to $\Delta f = \frac{2}{(3)(1 \cdot 10^{-3})}$ Hz $= 666.667$ Hz. Since in this example the bin size is much larger than the total frequency offset, the peak is sharp, falls in the right place and no chirp is present.

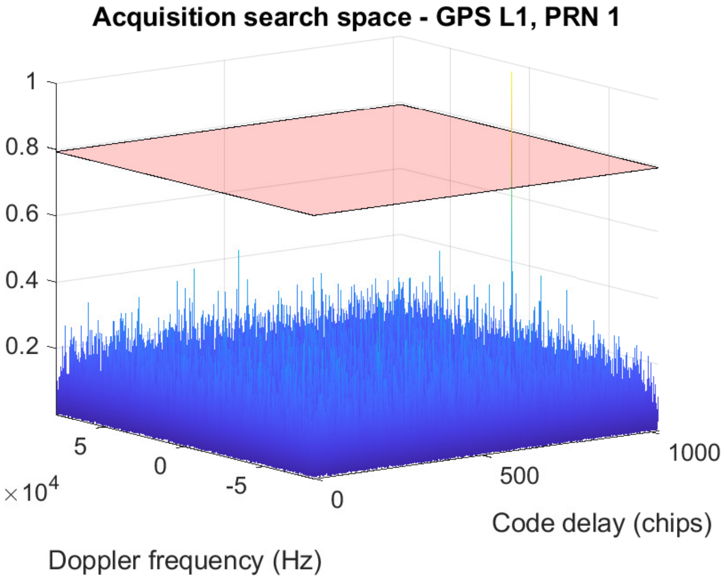

**Figure 3.3:** Acquisition without code Doppler and carrier Doppler rate compensation of a GPS L1 C/A code signal with $R_D = 1800$ Hz/s and $T_{coh} = 1$ ms. Plot of the normalized 3-D CAF.

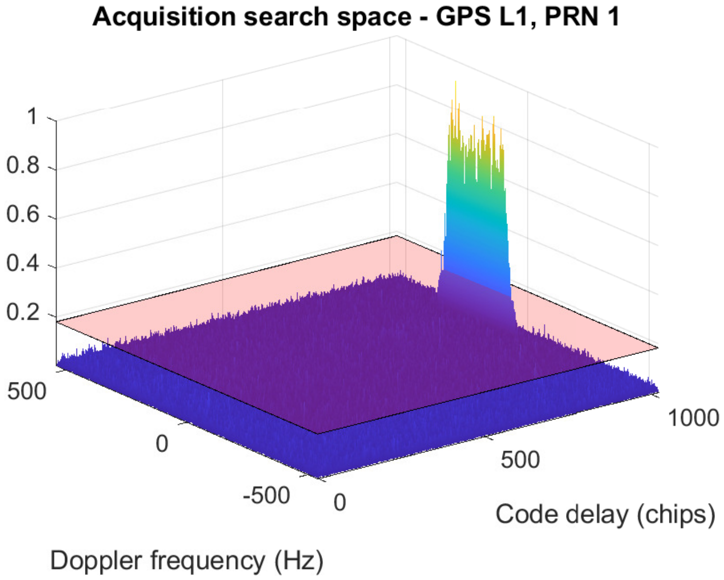

**Figure 3.4:** Acquisition without code Doppler and carrier Doppler rate compensation, of a GPS L1 C/A code signal with $R_D = 1800$ Hz/s and $T_{coh} = 150$ ms. Plot of the normalized 3-D CAF.

In the second example, an integration time of $T_{coh} = 150$ ms has been selected, implementing the coherent integration time extension technique. The correspondent Doppler bin size is $\Delta f = \frac{2}{(3)(150 \cdot 10^{-3})}$ Hz $= 4.444$ Hz, while the total frequency offset is equal to $R_D \cdot T_{coh} = 1800$ Hz/s $\cdot$ 150 ms $= 270$ Hz. Therefore, in this case the Doppler frequency bin size is much smaller than the total shift. In fact, as can be seen from the 3-D plot of the CAF in Fig. 3.4, it is evident the effect of the Doppler frequency changing over time, on the acquisition stage. In fact, a chirp starting from the initial value of the Doppler frequency $f_{D,0}$ and having a total length of about 270 Hz, is present in the Doppler frequency axis.

The size of the Doppler frequency bin is inversely proportional to the integration time interval, hence, a larger $T_{coh}$ corresponds to smaller $\Delta f$. Therefore, considering a fixed Doppler rate $R_D$, the larger $T_{coh}$, the smaller the bin size and the more evident is the drift of the correlation peak. Of course, the larger $R_D$, the larger the overall Doppler frequency shift and the longer is the chirp duration. To overcome this problem and to enable a good acquisition of the signal, not only the single carrier Doppler shift value, but also its change over time, must be estimated and compensated for. Hence, from now on it is assumed that the frequency aiding provided to the receiver concerns not simply an estimation of the Doppler frequency, but an estimation of the entire Doppler frequency profile $\mathbf{f}_D$, for a specific time interval. The Doppler profile is a collection of Doppler frequency values, evaluated at discrete time instants. This profile can be employed during the demodulation process.

In order to compensate the effect of the Doppler rate, a de-chirping must be implemented. The phase of the chirp is equal to the integral of (3.3):

$$\begin{aligned}\phi(t) &= \phi_0 + 2\pi \int_0^t f(x)dx \\ &= \phi_0 + 2\pi \int_0^t (rx + f_0)dx \\ &= \phi_0 + 2\pi \left(\frac{r}{2}t^2 + f_0 t\right)\end{aligned} \tag{3.4}$$

where $\phi_0$ is the initial phase at time $t_0$. This phase corresponds to the argument of the sinusoids used to perform the carrier wipe-off. In particular, the carrier wipe-off must be done considering the Doppler rate. According to (3.4), the complex sinusoid is equal to:

$$S = \exp\left\{ j2\pi \Big(\frac{R_D}{2}t + f_{D,0}\Big)t \right\} \tag{3.5}$$

In the acquisition stage, $f_{D,0}$ corresponds to the value to be tested $\bar{f}_c = f_{IF} + \bar{f}_D$. Moreover, the Doppler profile $\mathbf{f_D}$ is employed in the demodulation process, to compute for each sample the shift from $f_{D,0}$, and the resulting complex sinusoid is equal to:

$$S = \exp\left\{ j2\pi \bar{\mathbf{f}}_{\mathbf{c}} t \right\} = \exp\left\{ j2\pi \Big( (\frac{\mathbf{f_D} - f_{D,0}}{2}) + \bar{f}_c \Big) t \right\} \tag{3.6}$$

Therefore, what it is done in the acquisition stage is to sum, to each value to be tested $\bar{f}_c = f_{IF} + \bar{f}_D$, a vector representing, for each sample, the shift from the first sample, that is the initial value of the Doppler frequency shift. Thus, the test value of the Doppler frequency, corresponding to $\bar{f}_c = f_{IF} + \bar{f}_D$, becomes a vector of values $\bar{\mathbf{f}}_{\mathbf{c}} = \bar{f}_c + \Big(\mathbf{f_D} - f_{D,0}\Big)$. In this way, the Doppler frequency shift and the Doppler frequency shift rate are both compensated and the linear chirp is no more present in the output of the correlation funcion. In fact, as shown in Fig. 3.5, in the 3-D plot of the normalized CAF, the peak is present in the right bin, that is, based on the implemented compensation, the initial value of the Doppler frequency.

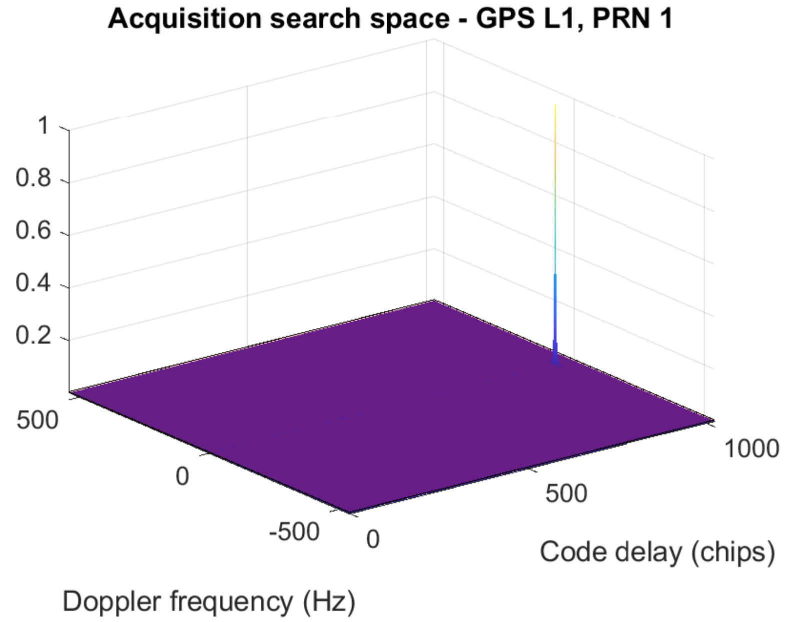

**Figure 3.5:** Acquisition with carrier Doppler rate compensation, of a GPS L1 C/A code with $R_D = 1800$ Hz/s and $T_{coh} = 150$ ms. Plot of the normalized 3-D CAF.

In fact, following (3.6), the Doppler frequency variation is compensated in such a way as to obtain the correlation peak in the bin corresponding to the initial Doppler frequency of the integration interval, that is $f_{D,0}$. This is just an implementation choice and it depends on the architecture of the tracking stage. This choice works well if the tracking stage processes the same snapshot of the signal processed by the acquisition. This happens in post-processing conditions and in snapshot positioning implementations. If instead the tracking exploits the following snapshot of the

signal, the acquisition should estimate the last value, in the integration interval, of the Doppler frequency shift.
Keeping the compensation implemented in (3.6), to obtain as estimation the last value in the interval of the Doppler shift, it is sufficient to sum the total Doppler shift to the initial value. In particular, in the software implementation of the digital signal processing stage, the acquisition stage provides to the tracking stage the vector index corresponding to the right Doppler frequency bin. Hence, to obtain the last value of the interval, this index must be shifted by the number of bins corresponding to the overall Doppler frequency shift:

```
$dopInd \leftarrow dopInd + \lfloor(\frac{(T_{coh}\cdot R_D)}{\Delta f})\rfloor$
$\hat{\tau}^{(a)} \leftarrow \text{dopplerFreqRange}[dopInd]$
```

where $(T_{coh} \cdot R_D)$ is the total shift in frequency and dividing it by the bin size gives the total shift in number of bins. The best implementation choice depends on the receiver and on the application.

## 3.2 Code Doppler

The Doppler frequency has an impact not only on the carrier frequency, but also on the code frequency. When the code-frequency offset is significant, the spreading code period suffers of a reduction or an expansion. This effect generates a code-chip slipping in the correlation process, producing an inconsistency between the local code phase and the phase of the received signal. Therefore, the output power of the correlation is reduced and this leads to a degradation of the acquisition performance.
The code Doppler shift depends on the Doppler frequency, the L1 carrier frequency (considering a GPS L1 signal) and the code frequency $R_{chip}$ and it is given by [27]:

$$f_{D,code} = \frac{f_D}{f_{L1}} R_{chip} \tag{3.7}$$

The actual chip rate of the received signal becomes:

$$R_{cd} = R_{chip} + f_{D,code} = R_{chip}\Big(1 + \frac{f_D}{f_{L1}}\Big) \tag{3.8}$$

depending on whether $R_{cd}$ is smaller or larger than $R_{chip}$, we have a stretch or a squeeze of the chip duration $T_c$ (Fig. 3.6). In fact, the resulting duration of the chip is:

$$T_{cd} = \frac{1}{R_{cd}} = T_{chip}\frac{1}{\Big(1 + \frac{f_D}{f_{L1}}\Big)} \tag{3.9}$$

A positive code Doppler shift leads to a shrink of the code duration, while a negative one causes an expansion of the code duration.
The received signal shifts of one chip, with respect to the local code, every $1/f_{D,code}$ seconds. Thus, there is a shift of 1 sample $T_s$ every $1/(f_{D,code} \cdot N_c)$ seconds (where $N_c$ is the number of samples per chip).

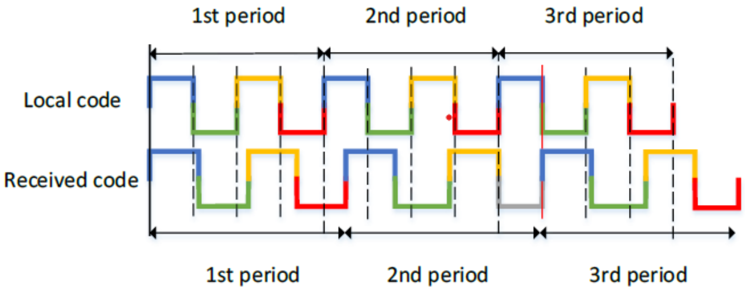

**Figure 3.6:** Effect of the code Doppler on 3 periods of a 4-chip spreading code. Picture taken from [28].

If the Doppler frequency shift is quite small, the code Doppler has not a great impact on the signal and thus, only the carrier Doppler can be taken into account. On the contrary, if the Doppler frequency is high, the effect of the code Doppler on the signal is significant. In fact, it generates a code-chip slipping in the correlation process, causing a degradation in the magnitude of the CAF and a shift of the true code delay [28]. Hence, as for the carrier Doppler, the code Doppler must be compensated for.

### 3.2.1 Code Doppler compensation

The GNSS receiver generates a local code replica to be correlated with the incoming signal, in order to estimate the code delay and Doppler frequency parameters. A possible way to compensate the code Doppler on the spreading code, is to generate this local replica by accounting for the effect of this Doppler. Of course, as for the carrier Doppler compensation, also in this case an external aiding it is necessary on the Doppler frequency profile. Having an estimate of the Doppler frequency profile of the incoming signal, the local code can be generated accordingly, with a code rate that depends on the incoming Doppler frequency (Eq. 3.8). In this way, the received signal and the local replica have the same number of samples in each code period. Hence, the misalignment between the local code and the incoming signal, due to the code Doppler, is compensated.
As for Sec. 3.1.1, a signal has been generated that has initial Doppler frequency shift equal to 40 kHz and Doppler frequency rate equal to 1800 Hz/s. According

to (3.7), the resulting code Doppler shift is therefore $f_{D,code} = 25.97$ Hz. This means that there is a shift of one chip, between the incoming signal and the local replica, every $1/f_{D,code} = 38.50$ ms. Therefore, if a short integration time is used, the phase slip caused by the code Doppler is negligible. On the contrary, if the acquisition stage requires more milliseconds, like in weak signal environments, the effect of the code Doppler is evident. Furthermore, it does not allow to benefit of the improvement in sensitivity given by using a longer integration time.

In view of the previous considerations, in order to show the effects of the code Doppler on the acquisition stage, and the results after compensating it, an integration time of $T_{coh} = 150$ ms is taken into account. Fig. 3.7 shows the XY plane of the 3-D CAF (that is the XY plane of Fig. 3.4), when there is neither the compensation of the Doppler shift rate nor of the code Doppler. In this plot, it is evident the shift of the true code delay, caused by the code-chip slipping. In fact, at the beginning of the integration time it is about 968.576 chips, while at the end of the interval is 963.871 chips. This effect is visible also looking at the 2-D plot of the CAF in the Doppler frequency domain, which is given fixing the value of the code delay to its best estimation. In fact, the peak appearing in this slice of the CAF, does not correspond to the shape of the chirp which is present on the plot of the 3-D CAF of Fig. 3.4. This is a further demonstration of the shift of the code delay.

When instead the compensation of the code Doppler is implemented, the shift of the code delay is no more present (Fig. 3.9). Indeed, the slice of the correlation function in the Doppler frequency domain (Fig. 3.10), presents the same shape visible in the plot of the 3-D CAF of Fig. 3.4.

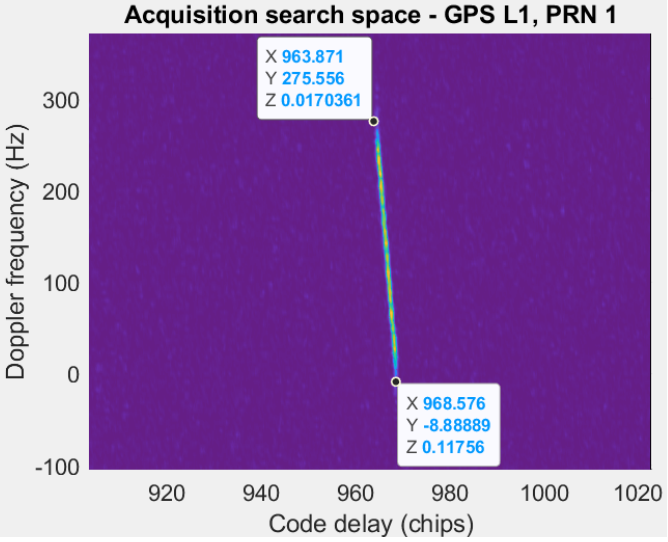

**Figure 3.7:** Acquisition without code Doppler and carrier Doppler rate compensation of a GPS L1 C/A code with $R_D = 1800$ Hz/s and $T_{coh} = 150$ ms. Plot of the X-Y plane of the normalized 3-D CAF.

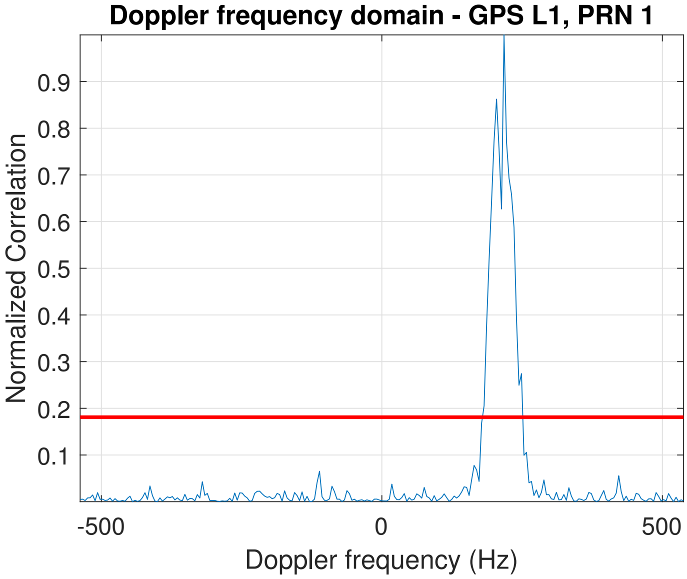

**Figure 3.8:** Acquisition without code Doppler and carrier Doppler rate compensation, of a GPS L1 C/A code with $R_D = 1800$ Hz/s and $T_{coh} = 150$ ms. Plot of the normalized 2-D CAF in the Doppler frequency domain.

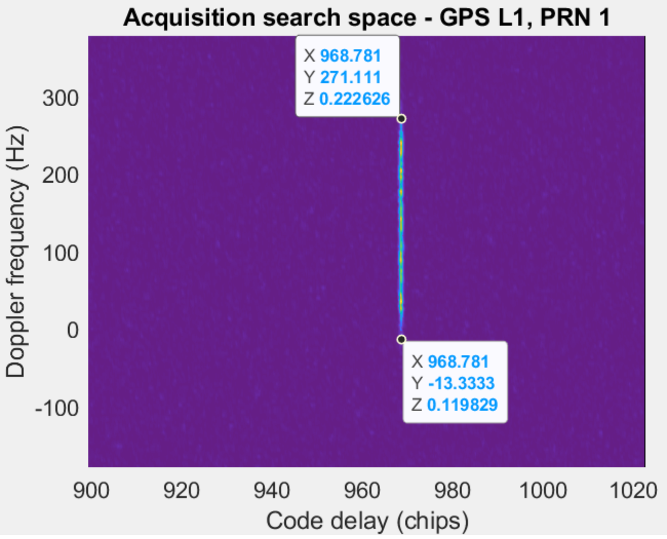

**Figure 3.9:** Acquisition with code Doppler compensation, of a GPS L1 C/A code signal having Doppler frequency rate equal to 1800 Hz/s, with $T_{coh} = 150$ms. Plot of the X-Y plane of the normalized 3-D CAF.

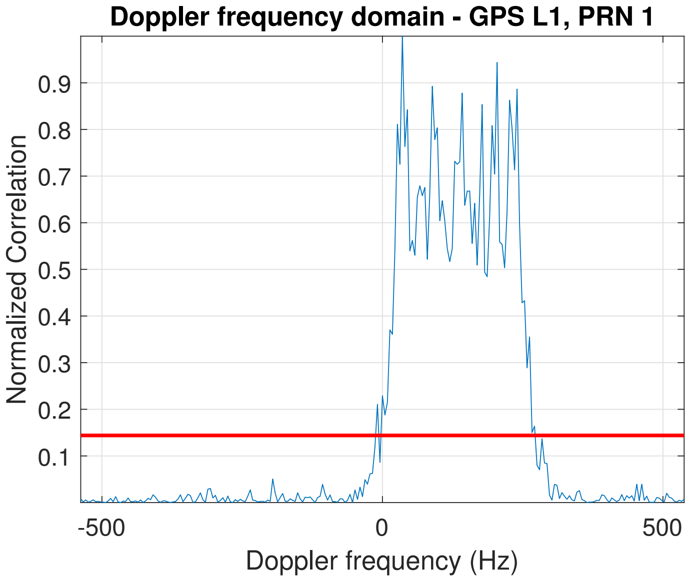

**Figure 3.10:** Acquisition with code Doppler compensation, of a GPS L1 C/A code signal having Doppler frequency rate equal to 1800 Hz/s, with $T_{coh} = 150$ms. Plot of the normalized 2-D CAF in the Doppler frequency domain.

A further interesting result regards the peak height with and without code Doppler compensation and its ratio with the noise floor. As shown in Table 3.1, with the code Doppler compensation the value of the peak is higher than without the compensation. In addition, the value of the noise floor is smaller in the case in which the compensation is implemented. Therefore, the ratio between the correlation peak and the noise floor is higher when the code Doppler is compensated. In particular the increment of the peak-to-noise ratio is about 35.79%.

**Table 3.1:** Values of the peak, noise floor, and peak-to-noise ratio of the correlation function, with and without the code Doppler compensation.

| | Without code Doppler compensation | With code Doppler compensation |
|---|---|---|
| Peak | $3.770 \cdot 10^{12}$ | $4.876 \cdot 10^{12}$ |
| Noise floor | $2.865 \cdot 10^{9}$ | $2.729 \cdot 10^{9}$ |
| $\frac{Peak}{Noisefloor}$ | 31.193 [dB] | 32.521 [dB] |

## 3.3 Signal de-noising

The compensation of the code and carrier Doppler allows to implement a sort of de-noising of the signal. In fact, after correctly demodulating the signal, it is possible to divide it into segments with length equal to that of the code being analysed. These segments can then be summed and finally be averaged. Specifically, considering a GPS L1 C/A code signal, it is divided into segments of 1 ms, which is the length of the period of the C/A code. Being the noise samples uncorrelated, thanks to this coherent accumulation, the noise is averaged and the shape of the code, even if still noisy, appears. Fig. 3.11 and Fig. 3.12 show the plot of the accumulation just described without and with code Doppler compensation respectively. In the first case, the code shape is not visible, while in the latter it emerges more clearly. Of course, the higher the $C/N_0$ at the input of the receiver, the clearer is the code shape. This operation is very useful because it allows to investigate phenomena which cause chip distortions such as multipath. In that case the code shape would not emerge clearly due to distortions.

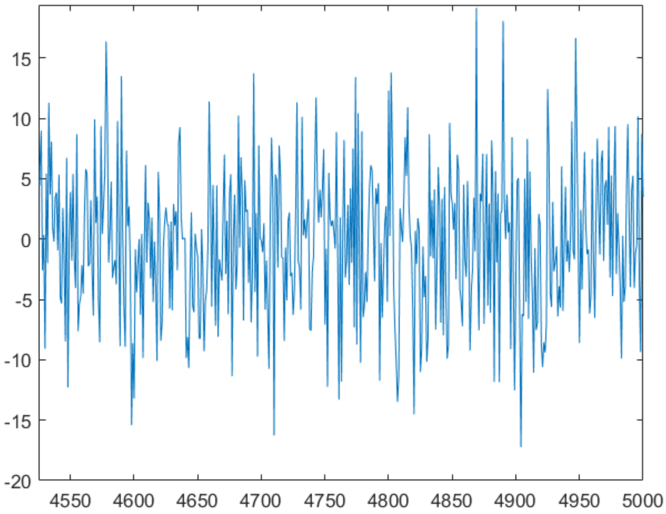

**Figure 3.11:** Signal de-noising without code and carrier Doppler compensation. Signal length = 50 ms.

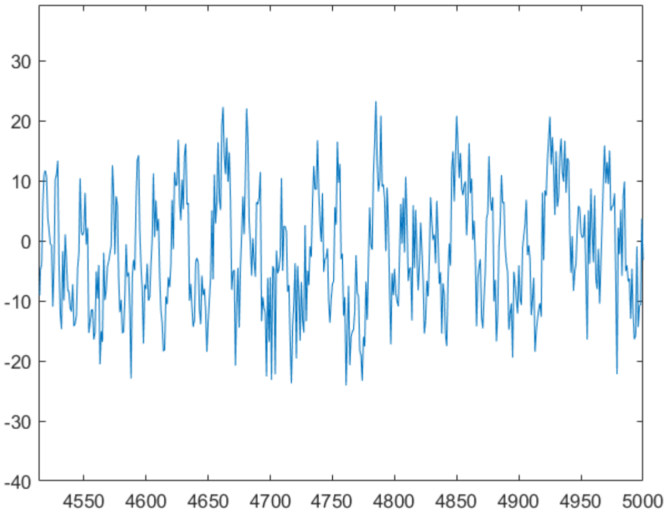

**Figure 3.12:** Signal de-noising with both code and carrier Doppler compensation. Signal length = 50 ms.

# Chapter 4

# The LuGRE project: a case study

The use of in-orbit GNSS receivers has been experimentally validated within the SSV, as in LEO and up to GEO altitudes. Latest missions, then, have unveiled GNSS performance for distances of about 150,000 km away from the Earth's surface. In fact, National Aeronautics and Space Administration (NASA)'s Magnetospheric Multiscale (MMS) has demonstrated the feasibility of tracking GPS signals up to this distance. The mission relied on four spacecraft supplied with high-sensitivity GPS equipment able to provide absolute position information. In its second phase their orbit reached 95,000 miles (152,900 km) from Earth, corresponding to about 41% of the Earth-Moon distance, and the record for the highest altitude fix of a GPS signal has been marked. Additionally, near the Earth, satellites reached a velocity of 22,000 miles per hour, which is the fastest known operational use of a GPS receiver [29]. MMS has demonstrated that future space missions can rely on GNSS even at very high altitudes, even tough current GNSSs were not designed for non-terrestrial use.

Discovering cis-lunar and lunar volume is becoming increasingly attractive because it represents the step towards the exploration of Mars. In this scenario, it is necessary to have a precise knowledge about spacecraft position. In the last years, many studies discussed the feasibility of using GNSS receivers for Moon Transfer Orbit (MTO) and lunar orbits. As an example, referring to the European Student Moon Orbiter mission, [30] analysed the possibility of using GNSS navigation for Earth-to-Moon missions. In particular, this study investigated the GPS and Galileo signal availability and the achievable $C/N_0$ levels, during different phases of the mission, considering an acquisition threshold of 35 dB-Hz. In [22], the design of a GPS L1 C/A receiver, as proof of concept of navigation system to reach the Moon, is described. The receiver, called WeakHEO, is composed by modules which are specific for the lunar scenario, characterized by high dynamics and low power signal. By processing RF signals generated by a GNSS simulator, it has been verified that this receiver is able to perform acquisition, tracking, data synchronization and demodulation of GPS L1 C/A signals down to 15 dB-Hz. An Orbital Filter (OF) is used to aid the acquisition and tracking stages and to increase the navigation accuracy up to few hundred meters at the Moon altitude. A technology enhancement of WeakHEO has been done developing the SANAG receiver, which shown the possibility of acquiring and tracking (down to 12 dB-Hz) Galileo and BeiDou signals as well. The main differences between WeakHEO and SANAF are given in [31].

These studies demonstrated that, with new technologies and strategies, it is possible to overcome the obstacles faced by spacecraft at high altitudes. As explained in Sec. 2.2.5, GNSS receivers should exploit an Orbital Filter, combining GNSS measurements with orbital models, to improve the navigation accuracy. A proper antenna pattern should be used at the spacecraft such that to maximize the signal reception. Moreover, specific acquisition strategies must be used, in order to increase the sensitivity of GNSS receivers and therefore to reach low $C/N_0$ levels. In Sec. 2.2, a set of techniques have been presented that are used for the acquisition of weak GNSS signals, in space applications. These techniques involve the extension of the integration time. However, when large integration time are used, if remarkable Doppler frequency and Doppler frequency rate are present, they have an impact on the acquisition stage. In [21], simulation results show that at the Moon altitude the carrier frequency is affected by a Doppler frequency shift up to 20 kHz and Doppler rate up to 4 Hz/s. Instead, at the beginning of the MTO, the Doppler shift reaches values up to 60 kHz, while the Doppler rate up to 65 Hz/s. Therefore, in order to make the receiver robust against these high dynamics, Doppler shifts and Doppler rates must be compensated, as addressed in Chapter 3. Once the Doppler is compensated, it is possible to apply the techniques allowing to increase the sensitivity of the acquisition stage.

In this Chapter, both Doppler compensation and high-sensitivity acquisition techniques have been validated through a GNSS software receiver. In particular, a real scenario has been analysed about a lunar mission. This project focuses on the development of a GNSS receiver with Software-Defined Radio (SDR) technology to support cis-lunar and lunar navigation. The receiver, namely Navigation Early Investigation on Lunar surface (NEIL), will stem from agreements between the NASA and the Agenzia Spaziale Italiana (ASI) and will be be developed by the Italian company Qascom. It will be integrated in the on-board payload of the Lunar GNSS Receiver Experiment (LuGRE), whose goal is to develop an activity in a lunar and cis-lunar environment. Its launch, through the SpaceX's Falcon 9 vehicle, is scheduled for the end of 2023 and it will land on the Moon's Mare Crisium basin [32]. As mentioned previously, the highest altitude fix of a GPS signal has been obtained in 2019 by NASA MMS spacecraft, almost half-way to the Moon. Therefore, NEIL is expected to be the first GNSS receiver in history providing positioning, about 400,000 km away from the Earth, through both GPS and Galileo signals. This will represent a big step toward a planned space station in lunar orbit, called Lunar Gateway, and future colonization of the Moon and then of Mars.

In the framework of the LuGRE mission, Qascom will develop a dual-frequency and dual-constellation GNSS receiver with a specific signal reception chain able to support the extreme condition of the Moon. This receiver will be part of the scientific payload of the NASA's Blue Ghost lunar lander at the beginning of 2022. As shown in Chapter 2, at high altitudes above the GNSS constellation, side lobes play an important role, since the main lobes are obstructed by the Earth, but they provide low-power signals in the receiver direction. Hence, the weak signals coming from GPS and Galileo antennas side lobes will be processed through proper techniques allowing positioning, navigation and timing on the journey to the Moon, in lunar orbits and finally on the Moon surface.

## 4.1 Simulations for different $C/N_0$

The main scientific goal of the LuGRE project is to deeply analyse the signals received by the GNSS receiver at higher altitudes, on its way to the Moon. For this purpose, the samples of the GNSS signal are saved and then transmitted by the GNSS receiver to ground stations, in order to be analysed in post-processing, as a scientific support. However, the GNSS payload has a limited storage capability which put a constraint on the length of the GNSS signal that has to be stored. Additionally, another limitation is due to the downlink window. In fact, besides the GNSS payload, the addressed mission involves other scientific payloads which share the downlink window. Therefore, it is important to limit the bit rate necessary to transmit the GNSS samples to ground and thus to limit the signal length. For example, given the Analogue-to-Digital Conversion (ADC) characteristics of the GNSS receiver, 150 ms of multi-frequency signals corresponds to about 5.4 MB of data to store and it requires a bit rate of 288 Mbps in order to be transmitted, which is practically unsuitable for the mission. Hence, this project foresees a technical limit on the length of the signal and, consequently, a bound on the extension of the integration time.

In light of these considerations, in the tests carried out in this thesis, a bound on the extension of $T_{coh}$ has been fixed to 150 ms. This bound is related to:

- Analyse acquisition capability employing techniques suitable for the *snapshot positioning* paradigm for spatial applications.
- Save and transmit, with the available resources, GNSS samples for ground post-processing to allow a complementary analysis of the behavior of GNSS receivers for space applications.

Considering the scenario just presented, some analyses have been carried out about the performance of an high sensitivity receiver. Specifically, requirements on $T_{coh}$ extension, for different $C/N_0$ levels, have been examinated, together with their compatibility with the mission technical bound. Additionally, it has been investigated how to improve performance changing the system and cell false alarm probability, $P_{FA}$ and $P_{fa}$, and reducing the number of Doppler frequency bins $N_D$ in the acquisition stage. It is assumed that an estimation of the Doppler profile is provided as external aiding and a compensation of the Doppler shift and the Doppler rate, both on the carrier and on the code, is implemented.
In view of these considerations, the performance of the acquisition stage, exploiting high sensitivity strategies, has been tested. In particular, coherent and non-coherent accumulation techniques have been utilized. Signals with different $C/N_0$ have been considered, corresponding to the different distances within the cis-lunar space. To do so, a polynomial model approximating the $C/N_0$ profile, depending on the distance from the Earth's centre, has been exploited. Specifically, the addressed scenario focuses on distances greater than those of the MEO orbits of the GNSS satellites. Hence, the model applies to these distances and $C/N_0$ values concerning distances smaller than the MEO orbits must not be taken into account. Fig. 4.1 shows the plot of the $C/N_0$ profile, given the model. The MEO region, where GNSS satellites are located, is highlighted in red. While the green line represents the distance of the Moon from the Earth. As can be seen from the $C/N_0$ curve, the higher the distance from the Earth, the lower the $C/N_0$ values. Actually, what must be considered is the distance from the GNSS constellation. Anyway, given the scale of involved distances, referring to the distance from Earth is a good enough approximation. The worst case scenario is at a distance of 60 RE, i.e. Earth-Moon distance, where the $C/N_0$ is about 18 dB-Hz.

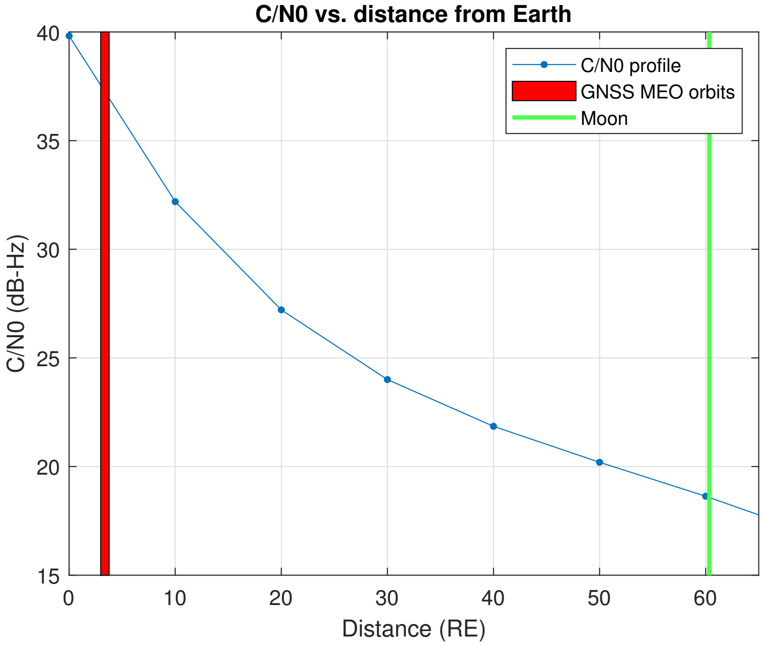

**Figure 4.1:** Approximate polynomial model of $C/N_0$ for distances included in the cis-lunar space. MEO GNSS orbits and Moon distance are highlighted as reference.

### 4.1.1 Acquisition performance depending on the size of Doppler frequency bins

In order to test the acquisition performance of the software receiver, a signal has been generated for each $C/N_0$ level of Fig. 4.1. Three different Search Space sizes have been taken into account, corresponding to three different number of Doppler frequency bins: $N_D = 3$, $N_D = 5$ and $N_D = 243$. In particular, $N_D$ can be reduced to few bins if an external aiding is provided to the receiver, e.g. by an Orbital Filter. In fact, supposing that an estimate of the Doppler profile is provided, the SS can be centred around the initial value of this profile, which is the initial value of $f_D$. Of course, the Doppler profile must be used also to implement the Doppler compensation shown in Chapter 3.

Initially, signals have been processed exploiting only coherent accumulation, introduced in Sec. 2.2. In that way, it has been possible to define, for each $N_D$, the requirements in terms of length of the coherent integration interval, that is, how many coherent sums M are needed for the acquisition. In Table 4.1, the number of coherent sums necessary to acquire the signals, for each size of $N_D$ and for different $C/N_0$ levels are reported. It is clear that, the smaller $C/N_0$, the larger must be $T_{coh}$ to be able to acquire the satellite. By setting a smaller $N_D$, which means reducing

the Search Space size, the value of $T_{coh}$ necessary to acquire signals is reduced too. This is due to the fact that the acquisition threshold B is fixed according to (1.21). In this equation, the single cell false alarm probability $P_{fa}$ is derived from (1.20), based on the system false alarm probability $P_{FA}$ (related to the entire SS). Hence, $P_{fa}$ depends on the total number of elements of the SS, which is equal to $N_\tau \times N_D$. The smaller the number of elements, the higher the $P_{fa}$ parameter is fixed, the smaller will be the value of the threshold. On the contrary, when the number of elements is higher, it is more probable that, due to the noise, the threshold is exceeded in a wrong bin. Therefore, in that case, the threshold is fixed to an higher value such that to have a smaller $P_{fa}$. If $P_{fa}$ is fixed to a specific value, instead of being computed based on $P_{FA}$, the value of the threshold is the same for every $N_D$. Anyway, for larger $N_D$ it is more probable that the signal acquisition occurs in a wrong bin.
The bound on the extension considered in this analysis is of $T_{coh} \leq 150$ ms. Fixing $P_{FA} = 10^{-3}$ and taking into account the limitation on $T_{coh}$, the acquisition of the signal is possible down to $C/N_0 = 21.852$ dB-Hz. This $C/N_0$ value corresponds to a distance of 40 RE, which is almost 70% of the Earth-Moon distance. Therefore, even with this limitation, it is possible to acquire the signal up to large distances. However, to acquire signals at the Moon distance, more samples of the signals must be processed, because an higher $T_{coh}$ is needed.

**Table 4.1:** Coherent sums: analysis of $T_{coh}$ needed for the acquisition for different values of $C/N_0$ and with different $N_D$. System false alarm probability fixed to $P_{FA} = 10^{-3}$.

| C/N0 [dB-Hz] | $T_{coh}$ [ms] ($N_D = 3$) | $T_{coh}$ [ms] ($N_D = 5$) | $T_{coh}$ [ms] ($N_D = 243$) |
|---|---|---|---|
| 39.821 | 2 | 2 | 2 |
| 32.191 | 6 | 7 | 8 |
| 27.211 | 41 | 43 | 60 |
| 24.004 | 89 | 89 | 121 |
| 21.852 | 100 | 100 | 107 |
| 20.197 | 157 | 158 | 175 |
| 18.634 | 228 | 368 | 418 |

In Tab. 4.2, the results about acquisition using the combination of coherent and non-coherent accumulations is shown. In particular, the length of $T_{coh}$ and the number of non-coherent sums K are reported. In all cases, the overall integration time required to acquired the signal is higher (or at most equal) with respect to the case in which only coherent sums are employed. Therefore, exploiting non-coherent accumulations does not add benefit in terms of required signal length to be processed. Non-coherent accumulations, suffer of the squaring loss [19]. In fact, the gain in noise reduction obtained with non-coherent strategy is lower with respect to the one given by coherent sums. However, non-coherent accumulations are useful when data-bit transitions are present. Additionally, when a large $T_{coh}$ is used, the Doppler frequency bin size $\Delta f$ is reduced. This could be a problem when there is an offset on the Doppler profile estimate, due to the uncertainty of the Orbital Filter. In fact, in this case, the smaller the bin size, the less probable is to acquire the peak as it will be clarified in Sec. 4.3.

**Table 4.2:** Combination of coherent and non-coherent sums: analysis of $T_{coh}$ and K needed for the acquisition for different values of $C/N_0$ and with different $N_D$. System false alarm probability fixed to $P_{FA} = 10^{-3}$.

| C/N0 [dB-Hz] | $T_{coh}$ [ms] ($N_D = 3$) | $T_{coh}$ [ms] ($N_D = 5$) | $T_{coh}$ [ms] ($N_D = 243$) |
|---|---|---|---|
| 39.821 | 1 (K=2) | 1 (K=2) | 1 (K=2) |
| 32.191 | 4 (K=2) | 4 (K=2) | 5 (K=2) |
| 27.211 | 15 (K=3) | 15 (K=3) | 15 (K=4) |
| 24.004 | 39 (K=3) | 40 (K=3) | 43 (K=3) |
| 21.852 | 26 (K=4) | 27 (K=4) | 30 (K=4) |
| 20.197 | 33 (K=5) | 33 (K=5) | 35 (K=6) |
| 18.634 | 150 (K=3) | 226 (K=2) | 300 (K=2) |

Both using coherent accumulation alone and combined with non-coherent one, having an integration interval with maximum length of 150 ms is not sufficient to acquire signals with $C/N_0 = 20.197$ dB-Hz, and $C/N_0 = 18.634$ dB-Hz, even using less Doppler frequency bins. Therefore, in order to reach these levels, besides $N_D$, it is necessary to adjust $P_{fa}$ and $P_{FA}$ parameters too.

### 4.1.2 Acquisition performance depending on the false alarm probability

The previous analyses on $T_{coh}$ have been done fixing the system false alarm probability to $P_{FA} = 10^{-3}$ and computing the cell false alarm probability from (1.20). $P_{FA}$ can be changed to find a proper value which allows to use a smaller $T_{coh}$, but maintaining a good acquisition accuracy. Another possible solution, is to directly fix the cell false alarm probability $P_{fa}$ to a specific value, instead of deriving it from the system false alarm probability $P_{FA}$. The larger this parameter is set, the smaller the threshold will be and the smaller $T_{coh}$ needed for the acquisition. Several tests have been made in both cases, to understand which are reasonable values for these parameters. Table 4.3 shows the required $T_{coh}$ to acquire signals with different $C/N_0$ levels, when $P_{FA}$ is the fixed parameter and $N_D = 3$. The last column corresponds to the first columns of Table 4.1, where $P_{FA} = 10^{-3}$. Increasing the system false alarm probability to $10^{-2}$ and $10^{-1}$ allows to acquire signals with a smallest integration time. In particular, with these larger values of $P_{FA}$, it has been possible to acquire with $T_{coh} \leq 150$ ms even the signal with $C/N_0 = 20.197$ dB-Hz. The same analysis have been carried out fixing the cell false alarm probability $P_{fa}$, instead of the system false alarm probability. Results are shown in Table 4.4. Also in this case, $T_{coh}$ needed for the acquisition is smaller than in Table 4.1.

**Table 4.3:** Coherent sums: analysis of $T_{coh}$ needed for the acquisition for different values of $C/N_0$, with $N_D = 3$. System false alarm probability $P_{FA}$ fixed to different values.

| C/N0 [dB-Hz] | $T_{coh}$ [ms] ($P_{FA} = 10^{-1}$) | $T_{coh}$ [ms] ($P_{FA} = 10^{-2}$) | $T_{coh}$ [ms] ($P_{FA} = 10^{-3}$) |
|---|---|---|---|
| 39.821 | 1 | 1 | 2 |
| 32.191 | 5 | 6 | 6 |
| 27.211 | 34 | 40 | 41 |
| 24.004 | 63 | 72 | 89 |
| 21.852 | 83 | 88 | 100 |
| 20.197 | 64 | 72 | 157 |
| 18.634 | 201 | 217 | 228 |

**Table 4.4:** Coherent sums: analysis of $T_{coh}$ needed for the acquisition for different values of $C/N_0$, with $N_D = 3$. Single cell false alarm probability $P_{fa}$ fixed to different values.

| C/N0 [dB-Hz] | $T_{coh}$ [ms] ($P_{fa} = 10^{-6}$) | $T_{coh}$ [ms] ($P_{fa} = 10^{-7}$) | $T_{coh}$ [ms] ($P_{fa} = 10^{-8}$) |
|---|---|---|---|
| 39.821 | 1 | 1 | 1 |
| 32.191 | 5 | 6 | 6 |
| 27.211 | 34 | 40 | 41 |
| 24.004 | 65 | 71 | 88 |
| 21.852 | 79 | 88 | 97 |
| 20.197 | 63 | 71 | 157 |
| 18.634 | 201 | 212 | 225 |

Both $P_{fa}$ and $P_{FA}$ parameters can be fixed depending on the requirements. Since in this scenario there is a bound on the extension of $T_{coh}$, it is useful to set a larger false alarm probability, so that the threshold is lower and acquisition is possible with a smaller $T_{coh}$. Anyway, it must be considered that, the higher these parameters are set, the more probable is to have a cell exceeding the threshold in a wrong bin. Hence, it could be a valid solution if there is a constraint on $T_{coh}$ and when $N_D$ is small. In fact, the less the number of bins, the less probable is that some values could give a false alarm, otherwise it could be risky. For example, performing the same tests with $N_D = 243$, in some cases the acquisition occurred in a wrong bin.

## 4.2 Frequency aiding: Doppler profiles

In Section 4.1, analyses about acquisition for different $C/N_0$ levels have been done generating and processing a GPS L1 signal, associated to GPS PRN 1, with fixed Doppler rate equal to 5 Hz/s. In this section, a more realistic scenario is illustrated. In fact, three slices of the Doppler profile experienced by a spacecraft on the MTO, with respect to GPS PRN 1 satellite, have been extracted through AGI Systems Tool Kit (STK). Figures 4.2b, 4.3b and 4.4b show the three Doppler profiles, related to intervals of 150 ms. In these short intervals, all the Doppler profiles are assumed holding a linear trend in time. The correspondent distances of the spacecraft from the Earth have been extracted too and they are illustrated in 4.2a, 4.3a and 4.4a. These slices are associated to different instants, which means different positions of the spacecraft on the orbit. Being related to the MTO, they can either approach the Earth or move away from it. In fact, for slices 1 and 2 the distance from Earth decreases, while for slice 3 it increases. Figures 4.5, 4.6 and 4.7 show the spacecraft location on the MTO for slice 1, slice 2 and slice 3 respectively. Three GPS L1 signals (PRN 1), characterized by these Doppler profile slices, have been generated and then processed by the software receiver. The latter, exploited the three profiles as frequency aiding for the acquisition engine.
The slice 1 is related to the instant in which the spacecraft is at a distance of about about 28.67 RE from Earth. Given this distance, the correspondent $C/N_0$ has been obtained through the model of Fig. 4.1 and is around 24.35 dB-Hz. The initial Doppler frequency, corresponding to the first sample of the profile, is 7353.69 Hz and the Doppler rate is about 2.25 Hz/s. Among the analysed Doppler profiles, slice 1 is related to the instant in which the spacecraft is closest to the GNSS constellation. In fact, it is characterized by an higher Doppler rate with respect to the others. Moreover, the correspondent $C/N_0$ is the highest as well.
Slice 2 is characterized by a distance from Earth of around 39.84 RE and the correspondent $C/N_0$ is 21.88 dB-Hz. The initial Doppler frequency is $-11497.55$ Hz, while the Doppler rate is $-0.14$ Hz/s.
Slice 3 is referred to the instant in which the spacecraft is at a distant of 58.61 RE

from the Earth, which is almost the Earth-Moon distance. Indeed, it is characterized by a low level of $C/N_0$, that is 18.86 dB-Hz. In this case the Doppler frequency starts from $-19430.11$ Hz and changes with a rate of 0.61 Hz/s.
As in the previous section, the length of $T_{coh}$ has been analysed that is required for acquiring the signals related to the 3 slices of Doppler profile. When the system false alarm probability is fixed to $10^{-3}$ and only coherent sums are exploited, it is possible to acquire the GPS satellite with $T_{coh} \leq 150$ ms only for the slice 1 (Table 4.5). Indeed, in that case the signal is acquired with $T_{coh} = 70, 70, 74$, when 3, 5 and 243 Doppler frequency bins are used respectively. For slice 2 just over 150 ms are needed, when $N_D = 3$ and $N_D = 5$. When instead $N_D = 243$ bins are used, the length of the coherent integration time needed for the acquisition is $T_{coh} = 179$ ms. As for slice 3, $T_{coh}$ is much larger than the bound. Using both coherent and non-coherent sums (Table 4.6), the results are similar to those of the previous section, meaning that the combination of these techniques does not allow to obtain a smaller overall integration interval. Therefore, also in this case, in order to obtain better results, cell and system false alarm probabilities must be increased. Indeed, setting $P_{FA}$ to $10^{-2}$ and $10^{-1}$ it has been possible to acquire the GPS signal, corresponding to slice 2, with an integration time smaller than 150 ms (Table 4.7). The same happened fixing $P_{fa}$ to $10^{-7}$ and $10^{-6}$, as can be seen in Table 4.8. Instead, signal associated to slice 3 requires a $T_{coh} > 150$ ms even with larger values of $P_{FA}$ and $P_{fa}$. Anyway, even for this signal the required $T_{coh}$ is reduced when larger $P_{fa}$ or $P_{FA}$ are used.

**Table 4.5:** Coherent sums: analysis of $T_{coh}$ needed for the acquisition for the 3 slices, with different $N_D$. System false alarm probability fixed to $P_{FA} = 10^{-3}$.

| Slice | C/N0 [dB-Hz] | $T_{coh}$ [ms] ($N_D = 3$) | $T_{coh}$ [ms] ($N_D = 5$) | $T_{coh}$ [ms] ($N_D = 243$) |
|---|---|---|---|---|
| 1 | 24.35 | 70 | 70 | 74 |
| 2 | 21.88 | 155 | 156 | 179 |
| 3 | 18.86 | 249 | 271 | 334 |

**Table 4.6:** Combination of coherent and non-coherent sums: analysis of $T_{coh}$ and K needed for the acquisition for the 3 slices, with different $N_D$. System false alarm probability fixed to $P_{FA} = 10^{-3}$.

| Slice | C/N0 [dB-Hz] | $T_{coh}$ [ms] ($N_D = 3$) | $T_{coh}$ [ms] ($N_D = 5$) | $T_{coh}$ [ms] ($N_D = 243$) |
|---|---|---|---|---|
| 1 | 24.35 | 25 (K=3) | 27 (K=3) | 51 (K=2) |
| 2 | 21.88 | 107 (K=2) | 109 (K=2) | 182 (K=2) |
| 3 | 18.86 | 183 (K=2) | 183 (K=2) | 190 (K=2) |

**Table 4.7:** Coherent sums: analysis of $T_{coh}$ needed for the acquisition for the 3 slices, with $N_D = 3$. System false alarm probability $P_{FA}$ fixed to different values.

| Slice | C/N0 [dB-Hz] | $T_{coh}$ [ms] ($P_{FA} = 10^{-1}$) | $T_{coh}$ [ms] ($P_{FA} = 10^{-2}$) | $T_{coh}$ [ms] ($P_{FA} = 10^{-3}$) |
|---|---|---|---|---|
| 1 | 24.35 | 63 | 67 | 70 |
| 2 | 21.88 | 109 | 121 | 155 |
| 3 | 18.86 | 199 | 221 | 249 |

**Table 4.8:** Coherent sums: analysis of $T_{coh}$ needed for the acquisition for the 3 slices, with $N_D = 3$. Single cell false alarm probability $P_{fa}$ fixed to different values.

| Slice | C/N0 [dB-Hz] | $T_{coh}$ [ms] ($P_{fa} = 10^{-6}$) | $T_{coh}$ [ms] ($P_{fa} = 10^{-7}$) | $T_{coh}$ [ms] ($P_{fa} = 10^{-8}$) |
|---|---|---|---|---|
| 1 | 24.35 | 62 | 66 | 70 |
| 2 | 21.88 | 105 | 121 | 154 |
| 3 | 18.86 | 195 | 208 | 247 |

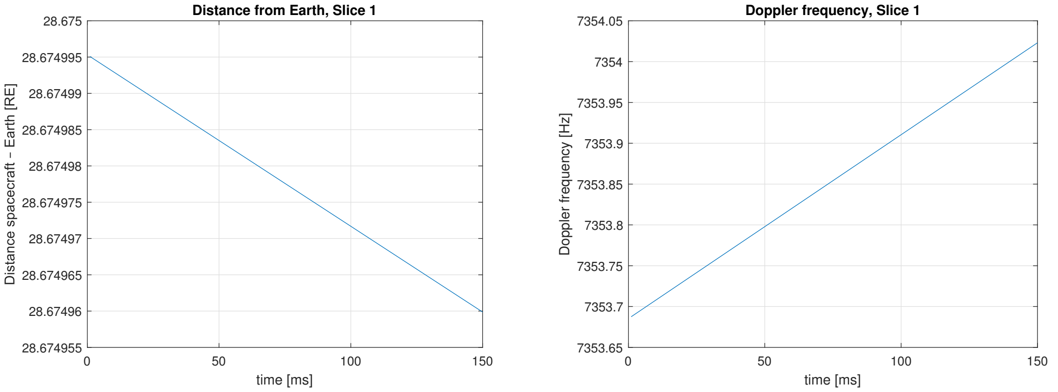

**(a)** Distance from Earth vs. time - Slice 1. **(b)** Doppler frequency vs. time - Slice 1.

**Figure 4.2:** Doppler frequency and distance from the Earth of a spacecraft in the MTO. Slice 1.

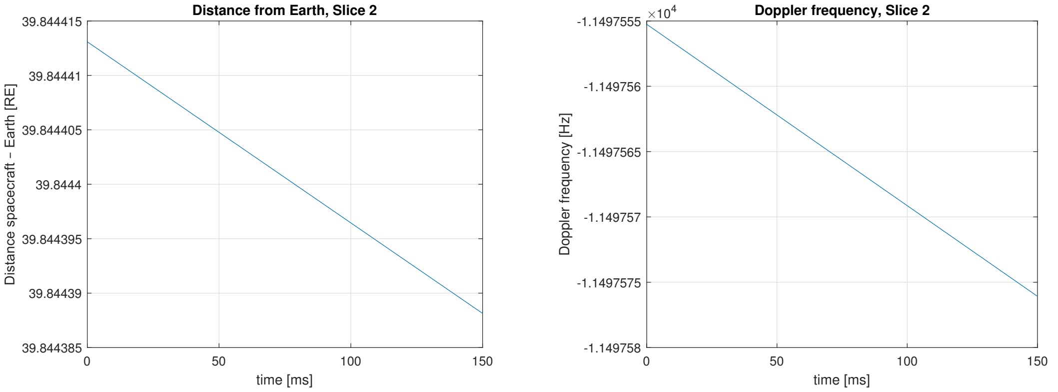

**(a)** Distance from Earth vs. time - Slice 2. **(b)** Doppler frequency vs. time - Slice 2.

**Figure 4.3:** Doppler frequency and distance from the Earth of a spacecraft in the MTO. Slice 2.

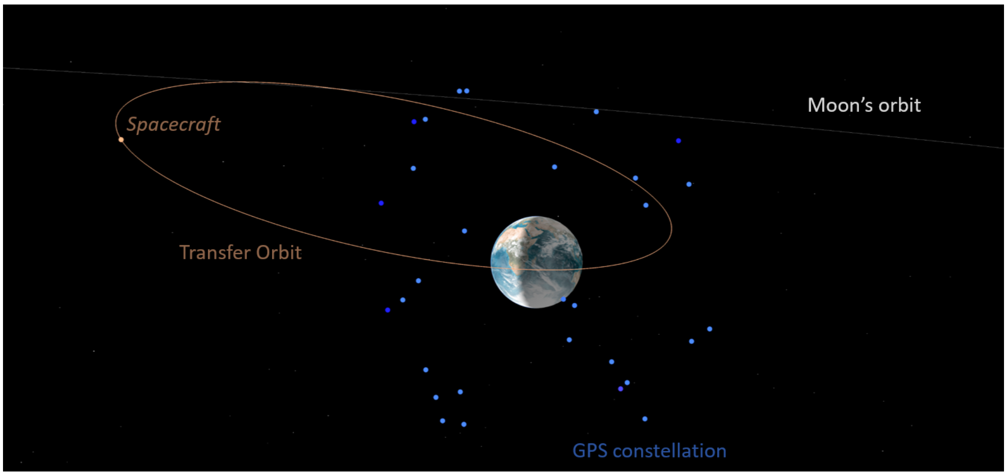

**Figure 4.5:** Spacecraft location on MTO - Slice 1.

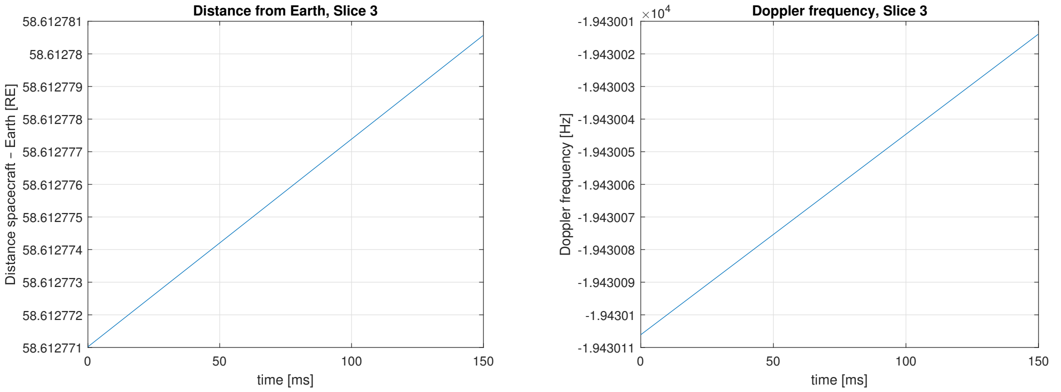

**(a)** Distance from Earth vs. time - Slice 3.

**(b)** Doppler frequency vs. time - Slice 3.

**Figure 4.4:** Doppler frequency and distance from the Earth of a spacecraft in the MTO. Slice 3.

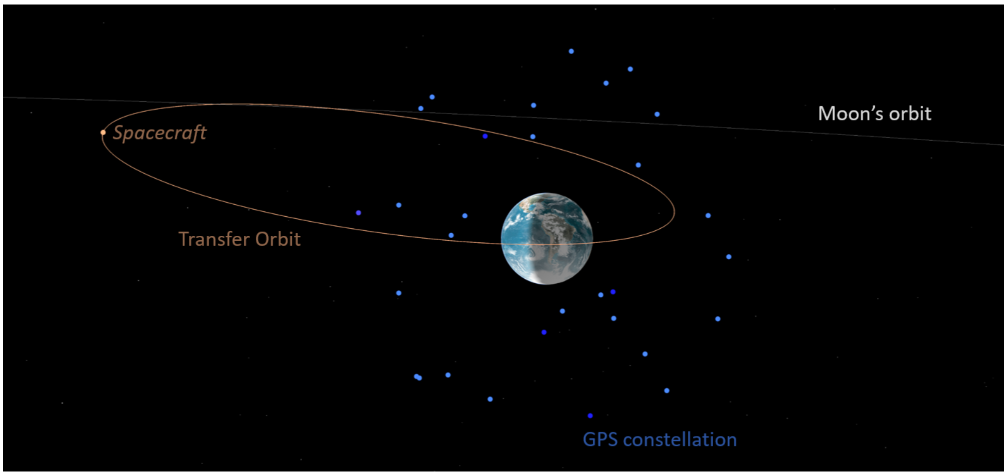

**Figure 4.6:** Spacecraft location on MTO - Slice 2.

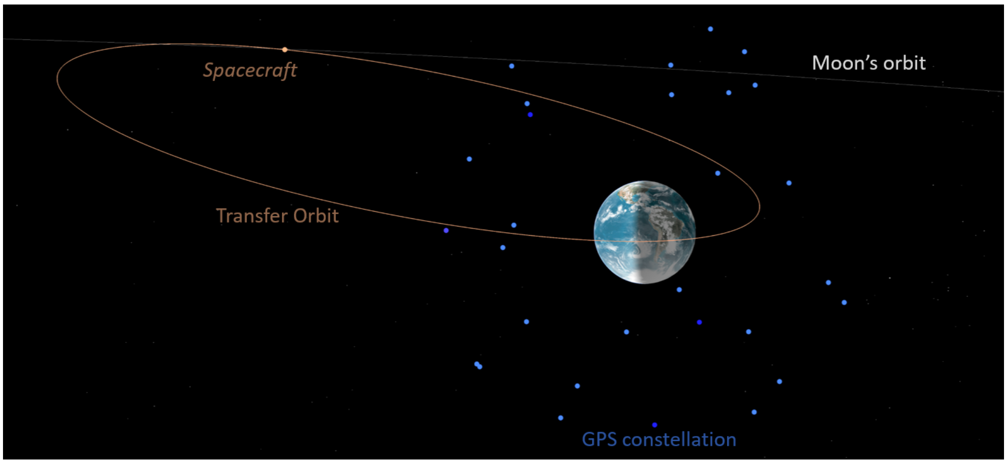

**Figure 4.7:** Spacecraft location on MTO - Slice 3.

## 4.3 Maximum acceptable offset for the Doppler profile

It has been shown that, in order to be able to compensate the Doppler frequency and Doppler frequency rate, an estimate of the Doppler profile must be provided to the acquisition stage. The correctness of this estimate depends on the Orbital Filter accuracy, thus, it is important to understand which are the effects on the acquisition when an error on the Doppler profile aiding is present. In particular, it has been analysed which are the consequences of an offset which causes a misalignment of the Doppler profile estimate with respect to the correct time. If the Doppler frequency changes linearly in time, or almost linearly, even if there is an offset (so if the Doppler profile is misaligned in time with respect to the correspondent snapshot of the signal) the compensation of Doppler rate presented in Chapter 3 still works. In fact, the implementation simply takes the difference between each sample and the first sample of the Doppler profile and, if the Doppler rate is almost constant, this difference is always the same. Hence, it is sufficient that the provided Doppler rate is correct. However, the estimation of the Doppler frequency is fundamental to reduce the number of Doppler frequency bins as well. In fact, the Search Space is centred around the initial value of the Doppler profile and the number of bins is reduced. Depending on the number of Doppler frequency bins $N_D$ to be tested and on the length of the integration interval $T_{coh}$, there is a different level of robustness against the frequency aiding error. $T_{coh}$ together with $N_D$, should be decided depending on the accuracy of the Orbital Filter. The more accurate is the Doppler frequency estimation, the smaller can be $N_D$. In general, the maximum acceptable error, so the maximum acceptable shift of the SS centre from the correct value, depends on the number of Doppler frequency bins to be tested and it is equal to:

$$\mathrm{MS}_{[bin]} = \frac{N_D - 1}{2} \tag{4.1}$$

Supposing that the Doppler profile, provided by the Orbital Filter, is subjected to a misalignment of $\mathrm{S}_{[s]}$ seconds, the correspondent shift in frequency is:

$$\mathrm{S}_{[Hz]} = R_D \cdot \mathrm{S}_{[s]} \tag{4.2}$$

While, the respective shift in number of bins is then:

$$\mathrm{S}_{[bin]} = \frac{\mathrm{S}_{[Hz]}}{\Delta f} \tag{4.3}$$

In the previous analyses, a bound on the extension of $T_{coh}$ has been considered. Having a fixed integration interval, allows to define the maximum acceptable offset. As an example, let's consider the Doppler profile 1, whose Doppler rate is about $R_D = 2.25$ Hz/s. If $T_{coh}$ is fixed to 150 ms, following the empirical rule (1.12), the Doppler frequency bin size $\Delta f$ is fixed too, and it is about 4.44 Hz. Based on the accuracy of the Orbital Filter and on $N_D$, different situations could happen. Supposing an offset on the Doppler profile of about $\mathrm{S}_{[s]} \simeq 7$ s, the respective shift in frequency is $\mathrm{S}_{[Hz]} \simeq 15.75$Hz. Due to this error, the SS is centred around the wrong value, which is the shifted one. Indeed, the peak in the CAF is not placed in centre of the SS, it is instead shifted of 3 bins. Depending on the value of $N_D$, different scenarios occur:

- $\mathbf{N_D = 243}$: since the SS is quite large, even if the correct value of $f_D$ shifts 3 bin away from the centre of the SS, it is still possible to find the peak and to acquire the satellite. Indeed, as shown in Fig. 4.8a, the peak is present for $\bar{f}_D = -13.33$ Hz. In fact, from (4.3), the shift in frequency from the right bin is exactly $\mathrm{S}_{[Hz]} = \mathrm{S}_{[bin]} \cdot \Delta f = 3 \cdot 4.44$ Hz $= 13.33$ Hz.

- $\mathbf{N_D = 5}$: the Doppler frequency range of the CAF is too small to contain the peak shifted from the centre due to the offset. In fact, it goes from $-8.89$ Hz to 8.89 Hz. Therefore, it is not possible to find the peak and the satellite is not acquired (Fig. 4.8b). According to (4.1), in order to be able to acquire the satellite, the shift caused by the error should be less or equal than 2 bins. Fig. 4.8d shows the plot of 2-D CAF in the Doppler frequency domain when a shift of 2 bins is caused by the frequency aiding error. The peak is in the first bin, corresponding to $-8.89$ Hz, and the satellite is correctly acquired.

- $\mathbf{N_D = 3}$: as for $N_D = 5$, with an offset of 3 bins, it is not possible to acquire the satellite. In this case, the CAF is characterized by a Doppler frequency domain going from $-4.44$ Hz to $4.44$ Hz (Fig. 4.8c). For $N_D = 3$, the maximum acceptable shift is only of 1 bin (4.1). Indeed, when the error of the Doppler profile estimate causes the shift of 1 bin, the peak is still present and the satellite can be acquired (Fig. 4.8e).

Since $T_{coh}$ is fixed to 150 ms and the Doppler rate is almost constant and equal to $R_D = 2.25$ Hz/s, for each value of $N_D$ it is possible to define the maximum shift in frequency and in time, starting from (4.1). For example, when $N_D = 5$, $\mathrm{MS}_{[bin]}$ is 2 bins. Therefore, from (4.3), $\mathrm{S}_{[Hz]} = 8.89$ Hz. Actually, all values up to about $f_D = 8.89 + \frac{\Delta f}{2}$ Hz will fall in that bins. Therefore, the maximum offset in frequency is $\mathrm{MS}_{[Hz]} = 11.11$ Hz. Instead, from (4.2), the maximum misalignment in time is $\mathrm{MS}_{[s]} = \mathrm{MS}_{[Hz]}/R_D \simeq 5$ s. Anyway, this is a particular case, with a specific constraint on $T_{coh}$, but in general, the maximum shift in frequency and time depends on:

- The length of the coherent integration time $T_{coh}$: if the empirical rule is used, $T_{coh}$ determines the Doppler frequency step, which means the size of the Doppler frequency bins. In particular, the larger $T_{coh}$, the smaller the Doppler frequency bin size. Therefore, it is even more risky employing a small value of $N_D$, because it is more probable that the peak shifts out of range.

- The Doppler rate: given a misalignment in time, the larger the Doppler rate, the larger the shift of the peak, the smaller should be the error.

Actually, besides the accuracy of the Orbital Filter, the shift is caused by the clock drift as well. In fact, the clock is not perfectly stable, and its drift causes an additional shift. Therefore, the total offset, which corresponds to the total shift from the right bin, is given by the error due to the aiding and the drift of the clock. The sum of these components must be within the maximum acceptable error.
To sum up, employing a smaller $N_D$ allows to reduce the $T_{coh}$ needed for the acquisition. The smallest $N_D$, the faster is the acquisition and the less processing and memory is required. However, the smallest is the acceptable error offset related to the Doppler profile estimate provided by the Orbital Filter. Therefore, a trade-off must be found between the performance of the acquisition and the computational effort of the GNSS receiver.

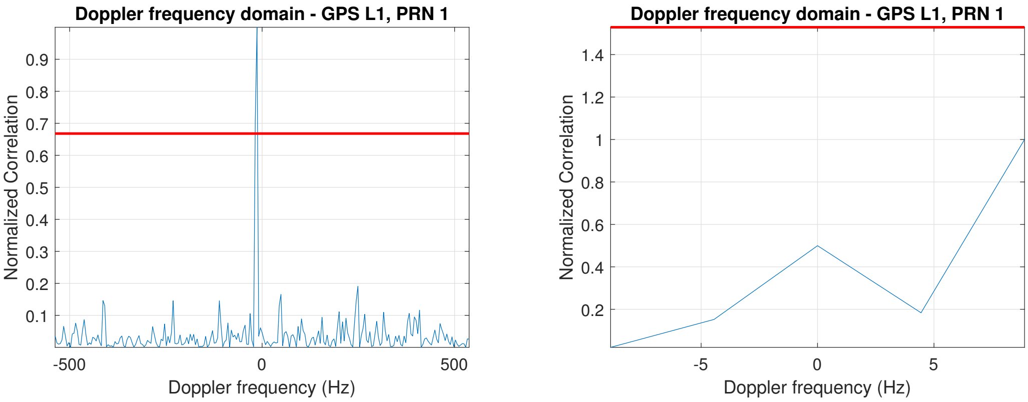

**(a)** Shift of 3 bins from the right $\bar{f}_D$. $N_D = 243$.

**(b)** Shift of 3 bins from the right $\bar{f}_D$. $N_D = 5$.

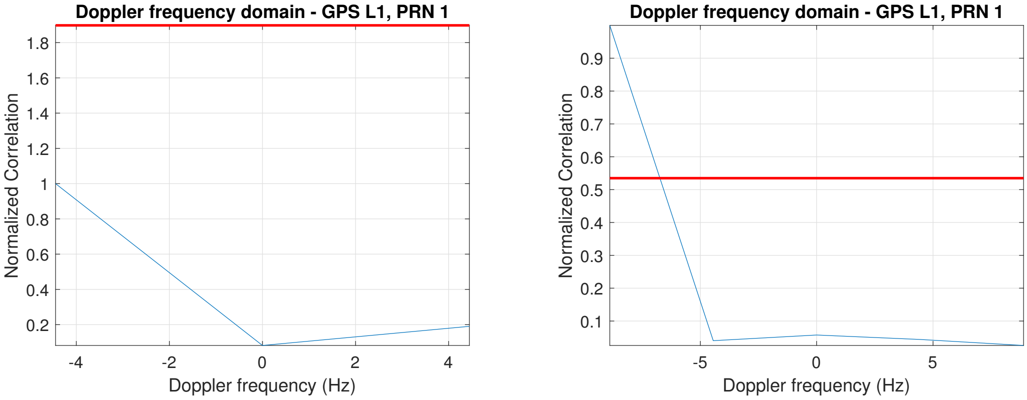

**(c)** Shift of 3 bins from the right $\bar{f}_D$. $N_D = 3$.

**(d)** Shift of 2 bins from the right $\bar{f}_D$. $N_D = 5$.

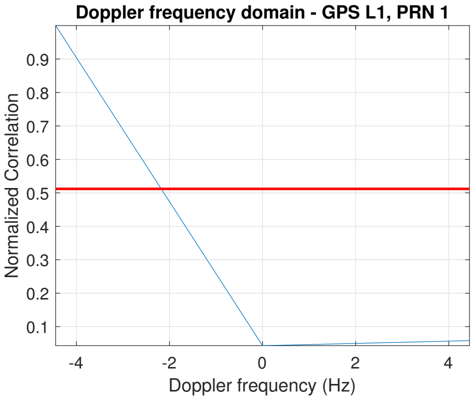

**(e)** Shift of 1 bins from the right $\bar{f}_D$. $N_D = 3$.

**Figure 4.8:** Acquisition of a GPS L1 C/A signal with $T_{coh} = 150$ ms in presence of a shift of the peak, due to an error of the frequency aiding.

# Chapter 5

# Conclusions

GNSS, originally designed to provide accurate Positioning, Navigation and Timing (PNT) information to terrestrial users, is going to be exploited for autonomous space navigation as well. Indeed, GNSS receivers in space, already validated in LEO, are now becoming attractive even for spacecraft navigation at larger distances, for example, in lunar missions. Exploiting GNSS as navigation system for spacecrafts approaching the Moon would easy several scientific experiments. In fact, relying on in-orbit GNSS-based navigation systems would make the space-craft more autonomous and would reduce the costs and the efforts of federated networks (e.g. NASA Deep Space Network (DSN) and the European Space Tracking Estrack network) providing tracking services. Additionally, it would pave the way to a planned space station in lunar orbit and future colonization of the Moon and then of Mars. Nevertheless, these altitudes represent a challenging environment, characterized by high Doppler frequency and very weak signals reception, compromising the performance of actual GNSS receivers, which were not designed for non-terrestrial navigation.

This work aimed at both analysing and implementing signal processing techniques allowing to increase the GNSS receiver sensitivity, to adapt its use to the space environment. These strategies involve the extension of the coherent integration time $T_{coh}$. However, by increasing $T_{coh}$, the effects of the Doppler on the signal are more evident, as shown in Chapter 3. In particular, the Doppler frequency and the Doppler frequency rate have an impact both on the central frequency and on the code frequency. The first, identified as carrier Doppler, causes a shift, continuously changing over time, between the transmitting frequency of the GNSS satellite and the GNSS receiver frequency. The second is the code Doppler and it causes a compression or an expansion of the code period, leading to an inconsistency between the local code phase and the phase of the received signal. These problems have been addressed in this thesis. Therefore, as a first step, a compensation of the carrier Doppler and the code Doppler has been designed, developed and validated through a software receiver. Such a compensation is done assuming that an estimate of the Doppler profile is provided by an Orbital Filter (OF). This frequency aiding is used also to centre the Search Space (SS) around the estimated Doppler frequency and to reduce the number of Doppler frequency bins $N_D$.

In order to test the Doppler compensation and the high sensitivity techniques presented during the course of this thesis work, a final chapter concerning a mission-case scenario has been reported. The addressed scenario is the LuGRE project, which focuses on an experimental assessment of the performance of a GNSS receiver to support cis-lunar and lunar navigation. This case study foresees a bound on the extension of the coherent integration time $T_{coh}$, due to a set of technical mission constraints. Taking into account this limitation, the acquisition performance has been analysed in terms of $C/N_0$ levels. In particular, three slices of the Doppler profile experienced by a spacecraft with respect to GPS satellites, on different positions in the Moon Transfer Orbit (MTO), have been considered.
Results highlighted the need, in the addressed scenario, for longer $T_{coh}$ than those employed for terrestrial applications. Specifically, coherent accumulation has been shown being more effective than non-coherent one, due to the squaring loss to which the latter is subject. Enlarging the integration time translates into the need for pilot channels (to avoid bit transitions) or lower bitrates than those currently used in the GNSS for the transmission of the navigation message. Additionally, long integration times requires the compensation of accumulated Doppler shift, to allow an effective acquisition and a correct initialization of the tracking loop.
Given the limitation on the extension of $T_{coh}$, the thesis work shown how to improve acquisition performance, in terms of required $T_{coh}$. It turned out that, reducing $N_D$ and setting the proper values of cell $P_{fa}$ and system $P_{FA}$ false alarm probabilities allows to acquire signals with a smaller $T_{coh}$. These analyses have also confirmed the fundamental importance of an accurate Doppler aiding information by the OF for the purpose of an effective reduction of the SS.
Based on the presented conditions and on the adopted models, the acquisition of GNSS signals is possible in the cis-lunar space and on the lunar surface. In order to finalize the prototyping of the Lunar GNSS software receiver, a further analysis of the tracking stage is needed to validate the overall effectiveness of the acquisition strategies implemented and analysed in this thesis. Future works can analyse the feasibility of dynamically setting the number of Doppler frequency bins $N_D$ and the length of the integration time $T_{coh}$ depending on the uncertainty of the OF.

# Bibliography

[1] GPS.gov. *Space Segment*. Official U.S. government information about the Global Positioning System (GPS). URL: https://www.gps.gov/systems/gps/space/ (cit. on p. 3).

[2] ESA - Navipedia. *GPS Space Segment*. [online]. 2011. URL: https://gssc.esa.int/navipedia/index.php/GPS_Space_Segment (cit. on p. 3).

[3] ESA - Navipedia. *GLONASS Space Segment*. [online]. 2011. URL: https://gssc.esa.int/navipedia/index.php/GLONASS_Space_Segment (cit. on p. 4).

[4] ESA - Navipedia. *Galielo Space Segment*. [online]. 2011. URL: https://gssc.esa.int/navipedia/index.php/Galileo_Space_Segment (cit. on p. 4).

[5] ESA - Navipedia. *BeiDou Space Segment*. [online]. 2011. URL: https://gssc.esa.int/navipedia/index.php/BeiDou_Space_Segment (cit. on p. 4).

[6] Elliott D Kaplan and Christopher Hegarty. *Understanding GPS/GNSS: principles and applications*. Artech house, 2017 (cit. on pp. 6, 8).

[7] ESA - Navipedia. *GNSS signal*. [online]. 2011. URL: https://gssc.esa.int/navipedia/index.php/GNSS_signal (cit. on pp. 6, 7).

[8] P. Misra and P. Enge. *Global Positioning System : Signals, Measurements, and Performance*. Revised Second Edition. Ganga-Jamuna Press, Dec. 2010. ISBN: 978-0-97095-442-8. URL: https://www.navtechgps.com/global-positioning-system-signals-measurements-and-performance-revised-second-edition-paperback/ (cit. on pp. 8–10, 21).

[9] ESA - Navipedia. *Front End*. [online]. 2011. URL: https://gssc.esa.int/navipedia/index.php/Front_End (cit. on pp. 10, 11).

[10] Ahmet Esat Süzer and Hakan Oktal. «PRN code correlation in GPS receiver». In: *2017 8th International Conference on Recent Advances in Space Technologies (RAST)*. 2017, pp. 189–193. DOI: 10.1109/RAST.2017.8002960 (cit. on p. 12).

[11] Daniele Borio, Laura Camoriano, and Letizia Lo Presti. «Impact of GPS acquisition strategy on decision probabilities». In: *IEEE Transactions on Aerospace and Electronic Systems* 44.3 (2008), pp. 996–1011. DOI: `10.1109/TAES.2008.4655359` (cit. on p. 18).

[12] J.H.J. Iinatti. «On the threshold setting principles in code acquisition of DS-SS signals». In: *IEEE Journal on Selected Areas in Communications* 18.1 (2000), pp. 62–72. DOI: `10.1109/49.821719` (cit. on p. 19).

[13] Marco Rao and Gianluca Falco. «How can pseudorange measurements be generated from code tracking». In: *Inside GNSS Mag* 7 (2012), pp. 26–33 (cit. on p. 21).

[14] United Nations Office for Outer Space Affairs. «Interoperable GNSS space service volume». In: *The Interoperable Global Navigation Satellite Systems Space Service Volume*. United Nations, 2019, pp. 7–10 (cit. on pp. 23, 24).

[15] Catherine L Thornton and James S Border. *Radiometric tracking techniques for deep-space navigation*. John Wiley & Sons, 2003 (cit. on p. 24).

[16] Jennifer E Donaldson, Joel JK Parker, Michael C Moreau, Dolan E Highsmith, and Philip D Martzen. «Characterization of on-orbit GPS transmit antenna patterns for space users». In: *NAVIGATION, Journal of the Institute of Navigation* 67.2 (2020), pp. 411–438 (cit. on p. 25).

[17] G. Impresario, G. D'Amore, C. Stallo, L. Ansalone, and A. Tuozzi. «GNSS and GALILEO for CIS-Lunar and Moon Navigation». In: *2018 IEEE 4th International Forum on Research and Technology for Society and Industry (RTSI)*. 2018, pp. 1–5. DOI: `10.1109/RTSI.2018.8548504` (cit. on p. 26).

[18] Reza Zekavat and R Michael Buehrer. *Handbook of position location: Theory, practice and advances*. Vol. 27. John Wiley & Sons, 2011 (cit. on pp. 27, 28, 30, 31, 35).

[19] Frank Stephen Tromp Van Diggelen. *A-gps: Assisted gps, gnss, and sbas*. Artech house, 2009 (cit. on pp. 28, 57).

[20] Fabio Dovis and Tung Ta. «High Sensitivity Techniques for GNSS Signal Acquisition». In: Feb. 2012. ISBN: 978-953-307-843-4. DOI: `10.5772/29453` (cit. on p. 30).

[21] Vincenzo Capuano, Paul Blunt, Cyril Botteron, and Pierre-André Farine. «Orbital Filter Aiding of a High Sensitivity GPS Receiver for Lunar Missions». In: Jan. 2016. DOI: `10.33012/2016.13422` (cit. on pp. 31, 52).

[22] Vincenzo Capuano, Paul Blunt, Cyril Botteron, Jia Tian, Jérôme Leclère, Yanguang Wang, Francesco Basile, and Pierre-André Farine. «Standalone GPS L1 C/A receiver for lunar missions». In: *Sensors* 16 (Mar. 2016), p. 347. DOI: `10.3390/s16030347` (cit. on pp. 32, 51).

[23] L. Musumeci, Fabio Dovis, João Silva, P.F. Silva, and Hugo Lopes. «Design of a High Sensitivity GNSS receiver for Lunar missions». In: *Advances in Space Research* 57 (Mar. 2016). DOI: `10.1016/j.asr.2016.03.020` (cit. on p. 32).

[24] Vincenzo Capuano. «GNSS-based Orbital Filter for Earth Moon Transfer Orbits». In: *Journal of Navigation* (Oct. 2015) (cit. on p. 32).

[25] P.F. Silva et al. «Weak GNSS signal navigation to the moon». In: vol. 4. Sept. 2013 (cit. on p. 32).

[26] Zheng Chenggong, Chen Xi, and Huang Zhen. «A comprehensive analysis on Doppler frequency and Doppler frequency rate characterization for GNSS receivers». In: *2016 2nd IEEE International Conference on Computer and Communications (ICCC)*. 2016, pp. 2606–2610. DOI: `10.1109/CompComm.2016.7925169` (cit. on pp. 35–37).

[27] XiaoPeng Jiao, Ju Wang, and Xiang Li. «High sensitivity GPS acquisition algorithm based on code doppler compensation». In: *2012 IEEE 11th International Conference on Signal Processing*. Vol. 1. 2012, pp. 241–245. DOI: `10.1109/ICoSP.2012.6491645` (cit. on p. 43).

[28] Myriam Foucras, Olivier Julien, Christophe Macabiau, and Bertrand Ekambi. «Detailed analysis of the impact of the code Doppler on the acquisition performance of new GNSS Signals». In: *Proceedings of the 2014 International Technical Meeting of The Institute of Navigation*. 2014, pp. 513–524 (cit. on p. 44).

[29] National Aeronautics and Space Administration (NASA). *MMS Orbit*. [online]. URL: `https://www.nasa.gov/mission_pages/mms/spacecraft/orbit.html` (cit. on p. 51).

[30] Giovanni Palmerini, Marco Sabatini, and Giorgio Perrotta. «En route to the Moon using GNSS signals». In: *Acta Astronautica* 64 (Feb. 2009), pp. 467–483. DOI: `10.1016/j.actaastro.2008.07.022` (cit. on p. 51).

[31] Paul Blunt, Cyril Botteron, Vincenzo Capuano, Saeed Ghamari, Mathieu Rico, and Pierre-André Farine. «Ultra-high sensitivity state-of-the-art receiver for space applications». In: Dec. 2016 (cit. on p. 52).

[32] Inside GNSS. *Italy and Qascom to Land First GNSS Receiver on the Moon*. [online]. URL: `https://insidegnss.com/italy-and-qascom-to-land-first-gnss-receiver-on-the-moon/` (cit. on p. 52).